

Stochastic Online Optimization for Cyber-Physical and Robotic Systems

Hao Ma^{1,2*}, Melanie Zeilinger² and Michael Muehlebach¹

¹*Learning and Dynamical Systems Group, Max Planck Institute for
Intelligent Systems, Max-Planck-Ring 4, Tübingen, 72076,
Baden-Württemberg, Germany.

²Institute for Dynamic Systems and Control, ETH Zürich,
Leonhardstrasse 21, Zürich, 8092, Zürich, Switzerland.

*Corresponding author(s). E-mail(s): hao.ma@tuebingen.mpg.de;
Contributing authors: mzeilinger@ethz.ch;
michael.muehlebach@tuebingen.mpg.de;

Abstract

We propose a gradient-based online optimization framework for solving stochastic programming problems that frequently arise in the context of cyber-physical and robotic systems. Our problem formulation accommodates constraints that model the evolution of a cyber-physical system, which has, in general, a continuous state and action space, is nonlinear, and where the state is only partially observed. We also incorporate an approximate model of the dynamics as prior knowledge into the learning process and show that even rough estimates of the dynamics can significantly improve the convergence of our algorithms. Our online optimization framework encompasses both gradient descent and quasi-Newton methods, and we provide a unified convergence analysis of our algorithms in a non-convex setting. We also characterize the impact of modeling errors in the system dynamics on the convergence rate of the algorithms. Finally, we evaluate our algorithms in simulations of a flexible beam, a four-legged walking robot, and in real-world experiments with a ping-pong playing robot.

Keywords: Gradient-Based Stochastic Optimization, Online Learning, Non-Convex Optimization, Reinforcement Learning, Cyber-Physical Systems, Robotic Control

1 Introduction

The increasing availability of sensors across various domains has led to the generation of vast volumes of data, ideal for analysis and training. However, a significant challenge arises from the traditional “Sampling-Training-Deployment” mode of machine learning algorithms. Once trained, most models remain static during deployment, unable to benefit from the continuous influx of new data. This limitation means that models risk becoming outdated as the environment evolves and new information emerges, leaving a substantial amount of potentially valuable data unused. This not only hinders improvements in performance but also falls short of enabling systems to continuously learn, adapt, and improve. Moreover, retraining models from scratch with new data is neither an economical nor a long-term solution. This issue is particularly prevalent in robotics, where deployed models struggle to adapt to ever-changing environments and continuous streams of new information and data.

1.1 Motivation

[Hazan and Singh \(2025\)](#) explore the challenge of controlling a drone to navigate from a source to a destination under unpredictable environmental conditions, such as weather and terrain. While indoor environments can be effectively managed using existing technologies, outdoor conditions present a significantly more complex problem, often requiring online adaptation. Not only does the environment in which a cyber-physical system operates constantly change (e.g. due to adverse weather conditions), but the system dynamics also drift over time. Factors such as battery degradation and mechanical wear gradually lead to performance deterioration. Thus, the conventional static “Sampling-Training-Deployment” paradigm in machine learning, which lacks online adaptivity, may severely limit performance of cyber-physical systems in complex environments.

A similar challenge is evident in reinforcement learning (RL). RL methods suffer from sample-inefficiency ([Laskin et al, 2020](#); [Heess et al, 2017](#); [Kalashnikov et al, 2018](#)) and are significantly impacted by the sim-to-real gap ([Shah et al, 2017](#); [Doso-vitskiy et al, 2017](#); [Furrer et al, 2016](#); [McCord et al, 2019](#)). Even for a static environment, trained models often require extensive fine-tuning before they can be successfully deployed in real-world applications, which requires extensive trial-and-error and human supervision, and might cause damage and unexpected harm.

To address these challenges, we propose a shift toward a new learning paradigm that enables cyber-physical systems to continuously learn from streaming data, allowing them to adapt to changing environments and non-stationary system dynamics in real time. This approach leverages online learning, a machine learning framework designed to efficiently incorporate data streams and update models dynamically, to overcome the limitations of the conventional “Sampling-Training-Deployment” paradigm enabling continuous performance improvement in complex real-world settings.

1.2 Online Learning

Online learning aims to minimize the expected regret as follows (Bubeck, 2012; Neu, 2015):

$$\text{Regret}(\mathcal{A}) = \mathbb{E} \left[\sum_{t=1}^T f(\omega_t; \zeta_t) \right] - \min_{\omega \in \Omega} \mathbb{E} \left[\sum_{t=1}^T f(\omega; \zeta_t) \right], \quad \zeta_t \stackrel{\text{i.i.d.}}{\sim} \mathcal{D}, \quad (1)$$

where \mathcal{A} denotes the online optimization algorithm that is used for performance optimization and f are stochastic loss functions, where the random variable ζ_t is independently and identically sampled from the unknown distribution \mathcal{D} . The expectation is taken with respect to the loss functions and the decision variables $\omega_t \in \Omega$. The decision variables ω_t are generated by the algorithm \mathcal{A} from a closed and convex set $\Omega \subseteq \mathbb{R}^{n_\omega}$, where $n_\omega \in \mathbb{N}_+$ denotes the number of decision variables ω . The loss functions f are typically assumed to be convex and bounded (Hazan, 2022; Shalev-Shwartz, 2012; Hall and Willett, 2015). However, one of the primary objectives of this article is to bridge the gap between theory and practice, enabling online learning algorithms to be deployed on cyber-physical systems. Therefore, in this article, we abandon the convexity assumption and instead rely on a more general smoothness assumption. In addition, T denotes the total number of iterations. Intuitively, we claim that an online optimization algorithm \mathcal{A} performs well if the regret induced by this algorithm is sub-linear as a function of T (i.e., $\text{Regret}(\mathcal{A}) = o(T)$), since this implies that on average, the algorithm performs as well as the best fixed decision variables $\omega^* = \arg \min_{\omega \in \Omega} \mathbb{E} \left[\sum_{t=1}^T f(\omega; \zeta_t) \right]$ in hindsight. Therefore, when T is large enough or tends to infinity, online learning can cope with continually growing streams of data at the algorithm level, so that the decision variables ω_t continuously improve performance.

Zinkevich (2003) was one of the first researchers to realize that simple gradient-descent strategies are effective at solving (1). Since then, a plethora of online learning algorithms have emerged and their effectiveness has been demonstrated in practical settings. These algorithms can be broadly categorized into two groups: The first group comprises algorithms that are targeted at linear loss functions, also referred to as the prediction with expert advice problem (Hazan, 2022; Abernethy et al, 2009; Shalev-Shwartz and Singer, 2007), with notable examples being the Follow the Leader (FTL) and Follow the Regularized Leader (FTRL) algorithms, as well as the hedge algorithm (Freund and Schapire, 1997; Littlestone and Warmuth, 1994; Muehlebach, 2023), and the Perceptron (Novikoff, 1962). Other online optimization algorithms have also been proposed to tackle the problem of prediction with expert advice, such as the exponentially weighted average forecaster and the Greedy Forecaster (Cesa-Bianchi and Lugosi, 2006), as well as the upper confidence bound algorithm (Auer et al, 2002). Compared to these online learning methods that are targeted to linear loss functions, gradient-based methods can handle more general loss functions and sometimes even achieve faster convergence rates (Ruder, 2017). In this article, we will focus on gradient-based online optimization and learning algorithms. Gradients

provide local information of the loss functions, which, compared to gradient-free algorithms, is known to expedite the convergence process (Nesterov and Spokoiny, 2017). However, in the stochastic programming problems that are considered herein, gradient information is often challenging or even impossible to obtain, which is why many RL algorithms rely, at their core, on zeroth-order optimization. In contrast, we advocate with our work the use of approximate, model-based gradients and demonstrate that even rough estimates are enough to achieve convergence. We also quantitatively characterize the impact of estimation errors on convergence and highlight that in contrast to zeroth-order methods, our rates are dimension independent.

Gradient-based online optimization algorithms can be further categorized based on whether higher-order derivatives are used. Examples of first-order gradient-based algorithms include the Passive-Aggressive Online Learning (Crammer et al, 2006), the approximate large margin algorithm (Gentile, 2000), the Online Mirror Descent (OMD) (Hazan, 2022; Bubeck, 2011), and the relaxed online maximum margin algorithm (Li and Long, 1999). Among these, the most widely employed algorithm is Online Gradient Descent (OGD) (Dekel et al, 2012; Hazan et al, 2007b,a; Kolev et al, 2023), which is summarized in Algorithm 1.

Algorithm 1: Online Gradient Descent

Input : initial parameters $\omega_1 \in \Omega$, iterations T , step length $\{\eta_t\}_{t=1}^T$
for $t = 1$ to T **do**
 IMPLEMENTATION: play ω_t and observe cost $f_t(\omega_t)$;
 UPDATE: $\hat{\omega}_{t+1} = \omega_t - \eta_t \nabla f_t(\omega_t)$;
 PROJECTION: $\omega_{t+1} = \Pi_\Omega(\hat{\omega}_{t+1})$;
end
Return: ω_{T+1}

We note that $\Pi_\Omega(\cdot)$ denotes the projection to the feasible set Ω , and is defined as follows:

$$\omega_t = \Pi_\Omega(\hat{\omega}_t) = \arg \min_{\omega \in \Omega} |\omega - \hat{\omega}_t|^2, \quad (2)$$

where $|\cdot|$ denotes the ℓ_2 -norm.

Sometimes, even faster convergence rates can be obtained with second-order methods, which not only require gradient information, but also the Hessian (Boyd and Vandenberghe, 2004; Nocedal and Wright, 2006). Examples include the second-order Perceptron (Cesa-Bianchi et al, 2005), the Confidence Weighted Learning (Dredze et al, 2008), the Adaptive Regularization of Weight Vectors (Crammer et al, 2013), and the Online Newton Step (ONS) (Hazan, 2022). However, in practical applications related to the control of cyber-physical systems, gradients are already difficult to obtain, let alone second-order information. In addition, second-order methods are plagued by the following shortcomings (Martens and Grosse, 2015; Reddi et al, 2019; Bottou, 2010; LeCun et al, 1998; Agarwal et al, 2017): i) the methods have a high computational complexity per iteration as they require assembling and inverting the Hessian, which is problematic for high-dimensional problems; ii) the methods can be sensitive to noise (inexact gradient and Hessian evaluation), which can result in oscillations or divergence. Thus, in this article, we introduce an efficient approximation

Table 1: Comparison of representative algorithms for online convex optimization, including their assumptions, regret bounds, and corresponding lower bounds.

Algorithm	Assumptions	Regret Bound	Lower Bound
FTRL	convex losses strongly convex regularizer	$\mathcal{O}(\ln T)$	$\Omega(\sqrt{T})$
FTRL	strongly convex losses strongly convex regularizer	$\mathcal{O}(\ln T)$	$\Omega(\ln T)$
OGD	convex losses bounded domain	$\mathcal{O}(\sqrt{T})$	$\Omega(\sqrt{T})$
OGD	strongly convex losses bounded domain	$\mathcal{O}(\ln T)$	$\Omega(\ln T)$
OMD	convex losses strongly convex mirror map	$\mathcal{O}(\sqrt{T})$	$\Omega(\sqrt{T})$
ONS	exp-concave or strongly convex losses	$\mathcal{O}(\ln T)$	$\Omega(\ln T)$

Abbreviations: FTRL: Follow-The-Regularized-Leader; OGD: Online Gradient Descent; OMD: Online Mirror Descent; ONS: Online Newton Step.

method for the Hessian matrix based on a trust-region method. Additionally, we provide a quantitative analysis of the sensitivity of our proposed second-order method to gradient estimation errors. A selection of the most important online learning algorithms, combined with their underlying assumptions and corresponding results, is summarized in Table 1.

1.3 Related Work

Online learning in cyber-physical systems and robotics, often referred to as online control, has long remained an underexplored area. Most of the existing work is confined to linear systems, typically in a setting where the dynamics of the system (and environment) are linear in both state and action, perturbed by Gaussian noise, and the loss function is quadratic in state and action, which corresponds to the well-known linear quadratic regulator (LQR) problem in control theory. When the system is unknown, researchers usually employ online learning algorithms to estimate the system parameters, then use tools from robust control theory to solve the LQR problem, thereby obtaining a linear feedback controller. For instance, [Abbasi-Yadkori et al \(2011\)](#) use online parameter estimation to achieve a control policy whose regret bound is $\mathcal{O}(T^{1/2})$. Under the same setting, [Dean et al \(2018\)](#) have introduced a computationally efficient alternative that attains a regret bound of $\mathcal{O}(T^{2/3})$, while also pointing out that achieving this rate requires the estimation errors of the system parameters to converge to a certain threshold. Moreover, [Cohen et al \(2019\)](#) reformulate the LQR problem as a convex semi-definite program, improving the regret bound to $\mathcal{O}(T^{1/2})$ while preserving computational efficiency, and the regret bound is growing cubically with the system dimension. [Mania et al \(2019\)](#) further relax the assumptions by considering that the system state is only partially observable, a setting with significant practical implications that we also adopt in our work, resulting in a regret bound nearly at $\mathcal{O}(T^{1/2})$. The regret bound explicitly depends on the error between the approximate

system and the true system, and achieving the proposed regret requires that this error is sufficiently small. All these approaches share the common paradigm of first estimating the system parameters online and then using control-theoretic tools to solve the LQR problem to obtain a linear feedback control policy.

In addition, [Abbasi-Yadkori et al \(2018\)](#) have proposed a model-free algorithm for controlling linear unknown systems subject to quadratic loss functions with theoretical guarantees. Numerical experiments demonstrate that this method dramatically outperforms standard policy iteration, although its performance is still inferior to that of a model-based approach, with a regret bound of $\mathcal{O}(T^{2/3+\xi})$ for any small $\xi > 0$, provided that the time horizon satisfies $T > C^{1/\xi}$ for some constant C . Moreover, the regret bound explicitly depends on the system dimension.

Various studies have explored alternative settings within the framework of linear systems. For example, a series of works assume that the loss function is adversarially chosen: [Abbasi-Yadkori et al \(2014\)](#) assume that the loss function remains quadratic but allows adversarially chosen tracking targets, with the system operating without noise. Since the system parameters are known, the proposed algorithm directly learns the control policy, achieving a regret bound of $\mathcal{O}((\log T)^2)$. Moreover, when the system transition dynamics are also adversarially chosen, the regret bound becomes $\mathcal{O}(T^{1/2})$. In this setting, the regret bound additionally scales logarithmically with the size of the set of linear policies. [Cohen et al \(2018\)](#) consider a linear time-invariant system with known (stochastic) dynamics, where the loss function remains quadratic but the parameters can be adversarially chosen. In this case, a gradient-based algorithm is proposed to directly learn the control policy online, yielding a regret bound of $\mathcal{O}(T^{1/2})$. Moreover, the regret bound scales sublinearly with the system dimension. [Cohen et al \(2018\)](#) provide simulation experiments evaluating this result where real-world data is used for the system dynamics while varying the costs and running the algorithms in simulation.

Another line of research has studied the convergence of different algorithms under adversarial settings, where the process noise is no longer stochastic but is instead composed of bounded adversarial disturbances, and any adversarial convex loss function is allowed. In this setting, traditional worst-case approaches in the control literature, such as \mathcal{H}_∞ control and its variants, tend to be overly pessimistic. For a known linear system, [Agarwal et al \(2019\)](#) employ a gradient-based algorithm to predict the weight matrix of the disturbance, thereby indirectly parameterizing the control input and achieving a regret bound of $\mathcal{O}(T^{1/2})$; [Hazan et al \(2020\)](#) extend this result to unknown systems, attaining a regret bound of $\mathcal{O}(T^{2/3})$; and [Yan et al \(2023\)](#) go even further by assuming that the system state is partially observable and use a gradient-free method, which results in a regret bound of $\mathcal{O}(T^{3/4})$. Their algorithm is evaluated in both synthetic linear and simulated nonlinear environments. It is worth noting that the regret bounds proposed in the aforementioned works all exhibit an explicit dependence on the system dimension.

In practice, however, most, if not all, systems are nonlinear. To address this, [Gradu et al \(2022\)](#) linearize a nonlinear system locally, transforming it into a time-varying linear system with bounded adversarial disturbances and adversarial convex loss functions. At the same time, [Gradu et al \(2022\)](#) employ the concept of adaptive regret

to handle changing environments. The algorithm implicitly tracks the locally optimal policy as the dynamics of the linear time-variant system change, and the adaptive regret achieves the bound of $\mathcal{O}(\text{OPT}^{1/2})$, where OPT denotes the cost of the best policy in hindsight over the entire horizon.

The paradigm of iterative system identification and control design has been studied in the adaptive control community for a long time, and various shortcomings have been pointed out (Anderson, 2005). An important shortcoming is that the identified system dynamics are only accurate for the given feedback controller that is applied in the identification step, and may not accurately describe the closed-loop dynamics when a different controller is applied, which may lead to unexpected results and failures. To address such scenarios with large model-uncertainty, Ho et al (2021) propose an alternative pipeline that uses only an approximate system dynamics and learns to control online. This idea aligns with our work, and we further quantitatively characterize the upper bound on system uncertainty allowed and its effect on convergence rates. Unlike traditional online control methods, Ho et al (2021) consider binary loss functions, where the cost is one when the system state and action do not meet a specified condition (indicating a mistake) and zero otherwise. The proposed algorithm is proven to incur only a finite number of mistakes in the long run, and simulation experiments (e.g., cart-pole swing-up) confirm this result. Furthermore, Lin et al (2024) introduce a meta-framework that simultaneously employs an online estimator for system parameters and online policy optimization for the controller. For a time-varying nonlinear system with Gaussian noise, this framework is shown to achieve a local regret bound of $\mathcal{O}(T^{5/6})$. Here, the local regret is defined as the sum of the norms of the partial derivatives of the loss function with respect to the state for each iteration; Lin et al (2024) argue that in nonconvex settings, this performance metric is more meaningful than traditional regret, and we adopt this metric in our work to characterize algorithm convergence. A detailed comparison of our work and related results is summarized in Table 2.

Despite the thorough and solid exploration of online control in previous studies, evaluations remain limited to simple numerical experiments. In robotics, online learning is often used for high-level planning tasks, rarely involving control policy learning (Bellicoso et al, 2018; Wang et al, 2022; Chignoli and Kim, 2021). This creates a significant gap between theory and practice. Our work bridges this gap by proposing a solution for online control of nonlinear systems, supported by real-world experiments. To the best of our knowledge, our work is pioneering in this regard.

1.4 Contribution

As we mentioned in Section 1.2, gradient-based methods enjoy faster convergence rates compared to gradient-free approaches, and this rate further improves with the use of higher-order derivatives, a point that Abbasi-Yadkori et al (2018); Agarwal et al (2019); Hazan et al (2020) confirms. However, very few studies in online control have applied gradient-based online learning in practice. We believe this is because, unlike in tasks such as text or image classification, obtaining gradients in the context of cyber-physical systems is particularly challenging. On the one hand, the system dynamics are often complex; on the other hand, the interactions with environments

Table 2: Comparisons of our work and previous ones regarding problem setups and results.

References	Unknown System	Loss Function	Disturbance	Partial Feedback	Modeling Error Analysis	Evaluation in Simulation	Evaluation in Real World	Regret
Methods for Linear Systems								
Abbasi-Yadkori et al (2011)	✓	quadratic	Gaussian	✗	✗	✗	✗	$\mathcal{O}(T^{1/2})$
Dean et al (2018)	✓	quadratic	Gaussian	✗	✗	✓	✗	$\mathcal{O}(T^{2/3})$
Cohen et al (2019)	✓	quadratic	Gaussian	✗	✗	✗	✗	$\mathcal{O}(T^{1/2})$
Mania et al (2019)	✓	quadratic	Gaussian	✓	✓	✗	✗	$\mathcal{O}(T^{1/2})$
Abbasi-Yadkori et al (2018)	✓	quadratic	Gaussian	✗	✗	✓	✗	$\mathcal{O}(T^{2/3+\xi})^a$
Abbasi-Yadkori et al (2014)	✗	quadratic adversarial	✗	✗	✗	✗	✗	$\mathcal{O}((\log T)^2)$
Abbasi-Yadkori et al (2014)	✓	quadratic adversarial	✗	✗	✗	✗	✗	$\mathcal{O}(T^{1/2})$
Cohen et al (2018)	✗	quadratic adversarial	known dynamics	✗	✗	✓	✗	$\mathcal{O}(T^{1/2})$
Agarwal et al (2019)	✗	convex adversarial	adversarial	✗	✗	✗	✗	$\mathcal{O}(T^{1/2})$
Hazan et al (2020)	✓	convex adversarial	adversarial	✗	✗	✗	✗	$\mathcal{O}(T^{2/3})$
Yan et al (2023)	✓	convex adversarial	adversarial	✓	✗	✓	✗	$\mathcal{O}(T^{3/4})$
Methods for Nonlinear Systems								
Gradu et al (2022)	✓	convex adversarial	adversarial	✗	✗	✗	✗	$\mathcal{O}(\text{OPT}^{1/2})^b$
Ho et al (2021)	✓	binary	✗	✗	✓	✓	✗	finite mistake bound ^c
Lin et al (2024)	✓	nonconvex adversarial	Gaussian	✗	✗	✓	✗	$\mathcal{O}(T^{5/6})^d$
Ours	✓	nonconvex stochastic	stochastic	✓	✓	✓	✓	$\mathcal{O}(T^{1/2})^e$

^aFor any small $\xi > 0$ and time horizon satisfies $T > C^{1/\xi}$ for a constant C .

^bOPT is the cost of the best policy in hindsight over the entire horizon.

^cThe convergence rate is characterized by the adaptive regret bound.

^dThe convergence rate is characterized by the local regret bound.

^eThe convergence rate is characterized by the local regret bound.

may be unknown, change over time, or difficult to model. In addition, some of our common assumptions in online learning settings tend to be ineffective, such as convexity of the loss functions, which often renders the theoretical guarantees vacuous. This explains why, despite its robust theoretical foundations, online control has rarely been implemented in real-world cyber-physical systems.

The purpose of this article is to bridge the gap between theory and practice in online control by proposing a framework that enables gradient-based online optimization algorithms to be directly applied to cyber-physical systems. Unlike most online control approaches, which typically perform online system identification followed by solving programming problems to derive control policies, we follow the idea of [Ho et al \(2021\)](#): we use an approximate model of the system and learn the control policy online. In contrast to [He et al \(2024\)](#); [Chan et al \(2025\)](#), which concentrate on feedback optimization in the online learning, our approach is applicable to both open-loop and closed-loop optimization settings. Our approach tolerates significant uncertainty in the approximate model, which is denoted by the modeling error modulus κ . We not only theoretically characterize an upper bound on κ and quantitatively assess its impact on convergence rates, but we also evaluate our theory through a variety of approximate models. Finally, building on the efficiency of quasi-Newton methods, under appropriate assumptions, our regret bound improves to $\mathcal{O}(T^{1/2})$. In addition, compared to the works of [Cohen et al \(2019\)](#); [Abbasi-Yadkori et al \(2018\)](#); [Cohen et al \(2018\)](#); [Agarwal et al \(2019\)](#); [Hazan et al \(2020\)](#); [Yan et al \(2023\)](#), our proposed regret bound no longer explicitly depends on the system dimension due to the use of approximate gradients. Our main contributions are summarized as follows:

- We propose an online control framework that utilizes an approximate model and employs gradient-based online optimization algorithms to learn control policies. This framework allows for significant model uncertainty, which is characterized by the modeling error modulus κ . We quantitatively analyze the impact of modeling errors on convergence, which is crucial for ensuring the applicability of our algorithms in real-world cyber-physical systems.
- We evaluate our conclusions through simulations and in real-world experiments¹. These include a flexible beam, a four-legged walking robot, and a ping-pong playing robot. The ping-pong playing robot is a real-world system that is powered by artificial pneumatic muscles. With our approach, the robotic arm is not only able to continually enhance the tracking performance but also resists the gradually changing dynamic characteristics of the system over time.
- We introduce a gradient-based online learning algorithm to learn the control policies, which encompasses both gradient descent and quasi-Newton methods through an appropriate parameter selection. In this algorithm, both the gradient and the quasi-Hessian matrix rely on approximate first-order gradient estimates. The quasi-Newton method demonstrates invariance to linear transformations of the decision variables, thus offering robustness in step size selection and achieving faster convergence compared to the gradient descent method. In contrast, the gradient descent algorithm has a significantly lower computational complexity per iteration, making it more suitable in conjunction with deep neural networks.

¹See the supplementary video for a demonstration of the experiments: <https://youtu.be/OLVvKGBa7PA>

- We prove convergence guarantees of the algorithms without convexity assumptions and rely only on smoothness assumptions. This ensures that our algorithms and conclusions are indeed applicable to a large class of real-world cyber-physical systems. Our convergence analysis requires an argument for decoupling the approximate Hessian matrix from its dependence on past random variables, which provides an important technical contribution, and achieves a (local) regret bound of $\mathcal{O}(T^{1/2})$.
- We establish the connection between our algorithms and real-world cyber-physical systems by learning feedforward and feedback controllers in the classic two-degrees-of-freedom control loop in an online manner. We derive the update schemes for our algorithms in both open-loop and closed-loop systems. Furthermore, the effectiveness of both open-loop and closed-loop approaches is evaluated through numerical experiments.

1.5 Structure

This article follows the structure outlined below: In Section 2, we will provide a detailed formulation of the stochastic programming problem addressed in this article. Subsequently, we will propose an algorithmic framework to solve this problem and characterize convergence rates in the presence of modeling errors. We will also discuss the assumptions required for proving the convergence results, whereby the detailed proofs are provided in Appendix A. In Section 3, we will motivate and discuss the proposed algorithms from the perspective of trust-region methods. Section 4 establishes the connection between our algorithms and real-world cyber-physical systems through the classic two-degrees-of-freedom control loop. In addition, we derive the update schemes for our gradient descent algorithm in both open-loop and closed-loop systems. The section highlights the capability of our algorithms to be directly deployed on real-world cyber-physical systems. In Section 5, our algorithms are applied to various cyber-physical and robotic systems, including a flexible beam, a four-legged walking robot and a ping-pong playing robot. The section further analyzes the tightness of our convergence results and the impact of the modeling errors on convergence. The section also provides detailed information about each example and highlights different methods that can be used for estimating gradients. The article concludes with a summary in Section 6.

2 Problem Setting: Stochastic Online Learning

We consider a specific form of (1), which is tailored to cyber-physical and robotic systems. We incorporate the system dynamics through the mapping G and parameterize actions (or control inputs) u_t via the function π . Both the dynamics G as well as the action parameterization π are added as constraints. Consequently, (1) is reformulated

as follows:

$$\begin{aligned}
& \mathbb{E}_{\zeta_t} \left[\sum_{t=1}^T l(y_t; \zeta_t) \right] - \min_{\omega \in \Omega} \mathbb{E}_{\zeta_t} \left[\sum_{t=1}^T l(y_t^*; \zeta_t) \right] \\
& \text{s.t. } y_t = G(s_0, u_t; \zeta_t), \quad y_t^* = G(s_0, u_t^*; \zeta_t) \\
& \quad u_t = \pi(\omega_t, y_t; \zeta_t), \quad u_t^* = \pi(\omega, y_t^*; \zeta_t), \quad \zeta_t \stackrel{\text{i.i.d.}}{\sim} p_\zeta,
\end{aligned} \tag{3}$$

where the constraints implicitly define y_t as a function of ω_t , s_0 and ζ_t , the superscript $(\cdot)^*$ denotes the optimal value in hindsight. The implicit equation arises due to the fact that feedback loops may potentially be present, and we assume that y_t exists and is well defined. The initial state of the cyber-physical system is denoted by $s_0 \in \mathcal{S} \subset \mathbb{R}^{n_s}$. The vectors $u_t = (u_{t,1}, \dots, u_{t,q})$ and $y_t = (y_{t,1}, \dots, y_{t,q})$ denote the input and output sequences of the cyber-physical system, such as a robot, where $u_{t,i} \in \mathcal{U} \subset \mathbb{R}^m$ and $y_{t,i} \in \mathcal{Y} \subset \mathbb{R}^n$, $i = 1, \dots, q$ represent the input and output at a certain time point i and at iteration t of the learning process. The mapping $G(\cdot, \cdot; \zeta) : \mathcal{S} \times \mathcal{U}^q \rightarrow \mathcal{Y}^q$ transforms a sequence of inputs into a sequence of outputs and represents the input-output behavior of the cyber-physical system. The input-output behavior is not necessarily deterministic, due to process, measurement, and actuation uncertainty, which is modeled with the random variable ζ_t . In practice, the mapping G is typically unknown and may exhibit a high degree of nonlinearity, for example due to friction in the joints of a robot. The mapping $\pi(\cdot, y_t; \zeta) : \Omega \rightarrow \mathcal{U}^q$ describes how the decision variables ω_t affect the controls u_t . The feasible set Ω is assumed to be closed and convex, and the function $l(\cdot; \zeta) : \mathcal{Y}^q \rightarrow \mathbb{R}$ describes the loss function, for example, tracking error, execution time, energy consumption, etc.

To facilitate understanding for the readers, we provide a detailed explanation of (3) using the drone example mentioned in Section 1.1 (Hazan and Singh, 2025). In this example, the random variable ζ represents all uncertain factors, such as terrain, wind, and rainfall, while G denotes the dynamics of the drone in the random environment. As we noted earlier, although indoor environments can be accurately modeled using existing techniques, modeling the dynamics outdoors, considering factors like terrain and weather, is often intractable. The output trajectory y of the drone typically includes its attitude and velocity trajectories, and we do not assume that the state trajectory of the drone is fully observable. The control policy model π , which we aim to learn online, generates the control policy u based on the drone output trajectory y , and may, in general, be affected by the random variable ζ . The loss function l is employed to evaluate the performance of the output trajectory y produced by a given control policy π ; for example, l can be a binary function that determines whether the drone safely reaches its destination, or it can be a nonconvex function derived from a cost map that assesses the quality of the flight path of the drone. Consequently, the regret defined in (3) quantifies the performance difference between the current control policy and the optimal policy in hindsight that would yield the best performance under any environmental conditions. By solving (3), we obtain a control policy π parameterized with the decision variable ω that enables the drone to perform well across varying terrain and weather conditions.

Another concrete but simplified example arises in autonomous driving, where the goal is to control a vehicle to avoid unpredictable hazards, such as sharp turns and obstacles, represented by the random variable ζ . The dynamics of the vehicle, unknown to the decision maker, are denoted by G , while the control policy π generates control actions u for hazard avoidance. The partially observable state trajectory of the vehicle is represented by y , including position, speed, direction, etc. The loss function l evaluates the risk faced in avoiding hazards ζ based on the outputs y , with successful avoidance resulting in zero loss. The regret defined in (3) characterizes the performance difference between the control policy and the optimal policy that would minimize risk over all unpredictable hazards. Employing online learning algorithms to solve (3) means that we learn the decision variables ω so that the controls minimize the risks faced in handling various emergency situations in autonomous driving.

Establishing a precise model of G is often a difficult task. Consequently, in this article, we adopt a black-box representation for G , avoiding any explicit characterization of its internal dynamics. Although the dynamic characteristics of G are unknown, we assume that G is differentiable with respect to u . Furthermore, we adopt the following notational convention: $\mathcal{G}(u_t)$ represents an approximation of the gradient of the mapping G at an input location, more precisely, $\mathcal{G}(u_t)$ denotes an approximation of $\partial G(s_0, u; \zeta) / \partial u|_{u=u_t}$ ². In the subsequent sections, we will demonstrate that even a rough approximation of $\partial G(s_0, u; \zeta) / \partial u|_{u=u_t}$ can serve as valuable prior knowledge, significantly improving the convergence rate of our algorithms.

To address the optimization problem (3), we propose Algorithm 2, which depending on the choice of ϵ represents either an online gradient descent or an online quasi-Newton method. We note that $(\cdot)^\dagger$ denotes the Moore-Penrose inverse.

In principle, the **projection** step from Algorithm 1 could be included to ensure that the parameters ω_t remain in Ω . However, in cyber-physical applications, $\pi(\omega, y; \zeta)$ typically represents a neural network, where the parameters have no direct physical interpretation. Constraints often occur on the inputs u , and arise, for example, from actuation limits. These can, however, be addressed by parameterizing the neural network in such a way that input constraints are automatically satisfied. In order to simplify the presentation, we will therefore omit the projection onto Ω , or equivalently set $\Omega := \mathbb{R}^{n_\omega}$. We now summarize the convergence guarantees of Algorithm 2 under the following assumptions:

Assumption 2.1 (*L-Smoothness*). *Let the loss functions $f(\cdot; \zeta) : \Omega \rightarrow \mathbb{R}$ be L -smooth, that is,*

$$|\nabla f(v; \zeta) - \nabla f(\omega; \zeta)| \leq L|v - \omega|,$$

for all $\omega, v \in \Omega$.

Assumption 2.2 (*Bounded Variance*). *There exists a constant $H \geq 0$ such that for all $\omega \in \Omega$ the following inequalities hold:*

$$\mathbb{E}_\zeta \left[|\nabla f(\omega; \zeta)|^2 \right] \leq H^2, \quad \mathbb{E}_\zeta \left[|\mathcal{F}(\omega; \zeta)|^2 \right] \leq H^2,$$

²The gradient approximation $\mathcal{G}(u_t)$ may depend on the realization of ζ_t . However, in order to simplify the notation we omit the dependency.

Algorithm 2: ONLINE-QUASI NEWTON METHOD

Input: initial parameters ω_1 , constant ϵ and α , iterations T , step length

$\{\eta_t\}_{t=1}^T$

for $t \leftarrow 1$ **to** T **do**

 SAMPLING: $\zeta \sim p_\zeta \rightarrow \zeta_t$;

 IMPLEMENTATION: $G(s_0, \pi(\omega_t, y_t; \zeta_t); \zeta_t) \rightarrow y_t$;

 EVALUATION: $l(y_t; \zeta_t)$;

 APPROXIMATION: $\mathcal{G}(u_t) \approx \partial G(s_0, \pi(\omega_t, y_t; \zeta_t); \zeta_t) / \partial u$;

 CALCULATION:

$$\mathcal{L}_t = \left(\mathbf{I} - \mathcal{G}(u_t) \frac{\partial \pi(\omega_t, y_t; \zeta_t)}{\partial y} \right)^\dagger \mathcal{G}(u_t) \frac{\partial \pi(\omega_t, y_t; \zeta_t)}{\partial \omega}; \triangleright \text{approximation of } \frac{\partial y_t}{\partial \omega_t}$$

$$\Lambda_t = \frac{1}{\epsilon} \mathcal{L}_t^\top \nabla_y^2 l(y_t; \zeta_t) \mathcal{L}_t + \frac{\alpha}{\epsilon} \nabla_\omega \pi(\omega_t, y_t; \zeta_t) \nabla_\omega \pi(\omega_t, y_t; \zeta_t)^\top + \mathbf{I};$$

$$A_t = \frac{1}{t} \sum_{k=1}^t \Lambda_k;$$

 UPDATE: $\omega_{t+1} = \omega_t - \eta_t A_t^\dagger \mathcal{L}_t^\top \nabla_y l(y_t; \zeta_t)$;

end

Return: ω_{T+1}

where $\mathcal{F}(\omega; \zeta)$ denotes the estimated gradient of $f(\omega; \zeta)$ induced by $\mathcal{G}(u)$, while $\nabla f(\omega; \zeta)$ denotes the true gradient, that is,

$$\mathcal{F}(\omega; \zeta) = \frac{\partial l(y; \zeta)}{\partial y} \left(\mathbf{I} - \mathcal{G}(u) \frac{\partial \pi(\omega, y; \zeta)}{\partial y} \right)^\dagger \mathcal{G}(u) \frac{\partial \pi(\omega, y; \zeta)}{\partial \omega},$$

$$\nabla f(\omega; \zeta) = \frac{\partial l(y; \zeta)}{\partial y} \left(\mathbf{I} - \frac{\partial G(s_0, u; \zeta)}{\partial u} \frac{\partial \pi(\omega, y; \zeta)}{\partial y} \right)^\dagger \frac{\partial G(s_0, u; \zeta)}{\partial u} \frac{\partial \pi(\omega, y; \zeta)}{\partial \omega}.$$

Assumption 2.3 (Bounded Hessian). *Given a sequence of single pseudo-Hessians Λ_t obtained according to Algorithm 2, there exists a constant $\lambda \geq 1$ such that for all $t = 1, \dots, T$ the following inequalities hold:*

$$1 \leq \lambda_{\min}(\Lambda_t) \leq \lambda_{\max}(\Lambda_t) \leq \lambda,$$

where λ_{\min} and λ_{\max} denote the minimum and maximum eigenvalues of a matrix, respectively.

In this work, we abandon the convexity assumption of the objective function f with respect to ω and employ a more general smoothness assumption instead (see Assumption 2.1). Assumption 2.1 and Assumption 2.2 are standard in non-convex optimization (Bottou et al, 2018). We note that the non-convexity of the objective function f arises from the nonlinear dynamics of the cyber-physical systems, while the function $l(y; \zeta)$ can still be chosen to be convex. Thereby, all additive terms in Λ_t in

Assumption 2.3 are guaranteed to be positive semi-definite. Furthermore, the matrix Λ_t depends on the parameter ϵ , which can always be chosen large enough, such that Assumption 2.3 is satisfied. Beyond this, we also make the following assumption on the modeling errors of our gradient estimate:

Assumption 2.4 (Modeling Error). *Let the parameters ω_t evolve according to Algorithm 2. There exists a constant $\kappa \in [0, 1)$ such that for all $t = 1, \dots, T$ the following inequality holds:*

$$|\mathbb{E}_\zeta [\mathcal{F}(\omega_t; \zeta) | \omega_t] - \mathbb{E}_\zeta [\nabla f(\omega_t; \zeta) | \omega_t]|^2 \leq \frac{\kappa^2}{\lambda} |\mathbb{E}_\zeta [\nabla f(\omega_t; \zeta) | \omega_t]|^2. \quad (4)$$

In fact, the parameter λ arises from choosing the ℓ_2 -norm in (4). If the inequality (4) is expressed in the metric $|\cdot|_{A_t^{-1}}$, the factor $1/\lambda$ can be avoided, where $|\cdot|_{A_t^{-1}}$ denotes the metric induced by the positive definite matrix A_t^{-1} , that is,

$$|x|_{A_t^{-1}}^2 := \sup_{|x| \leq 1} x^T A_t^{-1} x.$$

Then, we have the subsequent conclusions for Algorithm 2:

Theorem 2.1. *Let the loss functions $f(\cdot; \zeta) : \Omega \rightarrow \mathbb{R}$ satisfy Assumption 2.1 and Assumption 2.2, and let the pseudo-Hessian A_t satisfy Assumption 2.3. Let the estimate $\mathcal{G}(u_t)$ satisfy Assumption 2.4, and let the step size be chosen as*

$$\eta = \sqrt{\frac{2F(\omega_1)}{LH^2T}}.$$

Then the following inequality holds:

$$\frac{1}{T} \sum_{t=1}^T \mathbb{E}_{\zeta_{1:T}} \left[|\nabla F(\omega_t)|_{A_t^{-1}}^2 \right] \leq \sqrt{\frac{2LH^2F(\omega_1)}{(1-\kappa)^2 T}} + \frac{\lambda H^2 (\ln T + 2)}{(1-\kappa)T}, \quad (5)$$

where $\omega^* := \arg \min_{\omega \in \Omega} F(\omega)$ denotes the global optimum and $F(\omega) := \mathbb{E}_\zeta [f(\omega; \zeta)]$.

The proof of Theorem 2.1 is included in Appendix A. From the above conclusion, it is evident that even when using approximate gradients and avoiding convexity assumptions, the expected value of the average of the squared gradients still converges at a rate comparable to many popular stochastic optimization algorithms (Bottou et al, 2018). We note that, due to the unavailability of $\partial G(s_0, u; \zeta) / \partial u$ in practical scenarios, the convergence rate of Algorithm 2 needs to be characterized using the modeling error modulus κ , and the convergence rate is governed by $1/(1-\kappa)$. If the modeling error modulus κ reaches one, the results become trivial since the right-hand side in (5) becomes arbitrarily large. When the modeling error modulus κ is zero, it implies that the estimate $\mathcal{G}(u)$ has no bias. The intuitive representation of Assumption 2.4 in two-dimensional space is illustrated in Figure 1. The expectation of the gradient estimate $\mathbb{E}_\zeta [\mathcal{F}(\omega_t; \zeta) | \omega_t]$ lies within the open ball with center $\mathbb{E}_\zeta [\nabla f(\omega_t; \zeta) | \omega_t]$

and radius $|\mathbb{E}_\zeta[\nabla f(\omega_t; \zeta)|\omega_t|]/\sqrt{\lambda}$. This implies that Assumption 2.4 constrains the estimate $\mathbb{E}_\zeta[\mathcal{F}(\omega_t; \zeta)|\omega_t]$ both in magnitude and direction. Therefore, the parameter κ provides a reference for evaluating the quality of the obtained estimates.

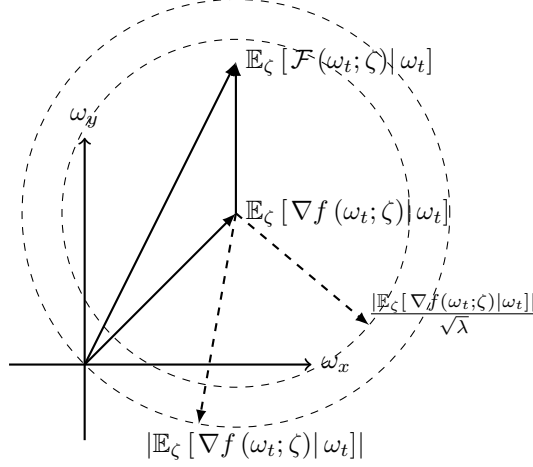


Fig. 1: This figure illustrates the geometric meaning of the modeling error modulus κ in two-dimensional space. The expectation of the gradient estimate $\mathbb{E}_\zeta[\mathcal{F}(\omega_t; \zeta)|\omega_t]$ lies within the open ball with center $\mathbb{E}_\zeta[\nabla f(\omega_t; \zeta)|\omega_t]$ and radius $|\mathbb{E}_\zeta[\nabla f(\omega_t; \zeta)|\omega_t|/\sqrt{\lambda}$.

We observe that by selecting a sufficiently large ϵ , the upper bound λ approaches one, thereby transforming Algorithm 2 from a Newton method to a gradient descent method. This suggests that by adjusting the value of ϵ , we can enable the algorithm to switch between Newton and gradient descent methodologies, leading to the following corollary:

Corollary 2.1. *Let the assumptions of Theorem 2.1 be satisfied and let $\epsilon \rightarrow +\infty$. Then, the following inequality holds:*

$$\frac{1}{T} \sum_{t=1}^T \mathbb{E}_{\zeta_{1:T}} \left[|\nabla F(\omega_t)|^2 \right] \leq \frac{\hbar_1}{\sqrt{T}} + \frac{\hbar_2 \ln T}{T} + \frac{2\hbar_2}{T},$$

where

$$\hbar_1 = \frac{\lambda \sqrt{2LH^2F(\omega_1)}}{1 - \kappa}, \quad \hbar_2 = \frac{\lambda^2 H^2}{1 - \kappa}.$$

Proof. According to Algorithm 2 we know that the matrix A_t is symmetric for all $t \geq 1$. In conjunction with Assumption 2.3, we conclude that the eigenvalues of A_t^{-1} are bounded below by $1/\lambda$ and above by unity for all $t \geq 1$. Consequently, the following inequality holds,

$$|\nabla F(\omega_t)|_{A_t^{-1}}^2 \geq \frac{1}{\lambda} |\nabla F(\omega_t)|^2, \quad \forall t \geq 1.$$

We insert the above inequality into (5), which yields the following inequality

$$\frac{1}{\lambda} \frac{1}{T} \sum_{t=1}^T \mathbb{E}_{\zeta_{1:T}} \left[|\nabla F(\omega_t)|^2 \right] \leq \sqrt{\frac{2LH^2 F(\omega_1)}{(1-\kappa)^2 T}} + \frac{\lambda H^2 (\ln T + 2)}{(1-\kappa)T},$$

and concludes the proof by multiplying by λ on both sides. \square

We note that A_t can be interpreted as an approximation of the Hessian matrix. Using its inverse as the metric to measure the norm of the gradient $\nabla F(\omega_t)$ in (5), guarantees the convergence criteria (and the algorithm) are invariant to linear transformations of the parameters ω_t . In the following experiments, we will observe that, compared to the gradient descent method, the quasi-Newton method is better at capturing the local curvature of the objective function, thus achieving more robust convergence and being insensitive to the step size η .

Next, we will reveal the connection between online learning and stochastic optimization, and provide the corresponding convergence guarantee. Prior to this, we make the following additional assumption:

Assumption 2.5 (Łojasiewicz Inequality). *There exists a constant $\mu > 0$ and an exponent $\theta \in (0, 1)$ such that for all $\omega \in \Omega$,*

$$|\nabla F(\omega)|^2 \geq 2\mu (F(\omega) - F(\omega^*))^{2\theta}. \quad (6)$$

Intuitively, this assumption says that near a critical point ω^* , the gradient $\nabla F(\omega)$ does not become too small relative to how close $F(\omega)$ is to its value at ω^* . The exponent θ reflects how “flat” or “steep” the function is around that point.

Additionally, we give the following definition measuring the distance to the minimum ω^* in Ω in terms of function value:

Definition 2.1. *The radius of the minimum $\omega^* \in \Omega$ is defined as*

$$\mathcal{D} := \sup_{\hat{\omega} \in \Omega} |F(\hat{\omega}) - F(\omega^*)|.$$

Then we show the following lemma:

Lemma 2.1. *Let Assumption 2.5 hold, then we have the following conclusions:*

1. *When $\theta \in (0, \frac{1}{2}]$, the following inequality holds*

$$\frac{1}{T} \sum_{t=1}^T (F(\omega_t) - F(\omega^*)) \leq \frac{\mathcal{D}^{1-2\theta}}{2\mu T} \sum_{t=1}^T |\nabla F(\omega_t)|^2, \quad (7)$$

where \mathcal{D} is defined in Definition 2.1.

2. *When $\theta \in (1/2, 1)$, the following inequality holds*

$$\frac{1}{T} \sum_{t=1}^T (F(\omega_t) - F(\omega^*)) \leq \left(\frac{1}{2\mu} \right)^{\frac{1}{2\theta}} \left(\frac{1}{T} \sum_{t=1}^T |\nabla F(\omega_t)|^2 \right)^{\frac{1}{2\theta}}. \quad (8)$$

Proof. For $\theta \in (0, 1/2]$, we note that for all $t \geq 1$ the function $\xi^{2\theta}$, $\xi \in [0, 1]$, is concave, which implies that

$$\frac{F(\omega_t) - F(\omega^*)}{\mathcal{D}} \leq \left(\frac{F(\omega_t) - F(\omega^*)}{\mathcal{D}} \right)^{2\theta}, \quad \forall t \geq 1,$$

where we use the fact that

$$0 \leq \frac{F(\omega_t) - F(\omega^*)}{\mathcal{D}} \leq 1, \quad \forall t \geq 1.$$

Combining with (6) yields

$$\frac{F(\omega_t) - F(\omega^*)}{\mathcal{D}} \leq \frac{1}{\mathcal{D}^{2\theta}} |\nabla F(\omega_t)|^2, \quad \forall t \geq 1.$$

Finally, we conclude the proof of (7) by summing both sides over t from one to T .

For $\theta \in (1/2, 1)$, we note that for all $t \geq 1$ the function $\xi^{2\theta}$, $\xi \geq 0$, is convex, which yields that

$$\left(\frac{1}{T} \sum_{t=1}^T (F(\omega_t) - F(\omega^*)) \right)^{2\theta} \leq \frac{1}{T} \sum_{t=1}^T (F(\omega_t) - F(\omega^*))^{2\theta}$$

by applying Jensen's inequality. Then combining with (6), we have

$$\left(\frac{1}{T} \sum_{t=1}^T (F(\omega_t) - F(\omega^*)) \right)^{2\theta} \leq \frac{1}{2\mu} \frac{1}{T} \sum_{t=1}^T |\nabla F(\omega_t)|^2.$$

Finally, we conclude (8) by raising both sides to the power of $1/2\theta$. \square

Following Assumption 2.5, we have the conclusions:

Corollary 2.2. *Let the assumptions in Theorem 2.1 be satisfied, and let Assumption 2.5 hold. Then, for any $\epsilon > 0$, the following results hold:*

1. *When $\theta \in (0, 1/2]$, the expected regret satisfies the inequality:*

$$\mathbb{E}_{\zeta_{1:T}} \left[\sum_{t=1}^T f(\omega_t; \zeta_t) \right] - \min_{\omega \in \Omega} \mathbb{E}_{\zeta_{1:T}} \left[\sum_{t=1}^T f(\omega; \zeta_t) \right] \leq \frac{\hbar_1 \sqrt{T} + \hbar_2 \ln T + 2\hbar_2}{2\mu \mathcal{D}^{2\theta-1}}. \quad (9)$$

In addition, let $\delta \in (0, 1)$, then the following inequality on the online regret holds with probability $1 - \delta$:

$$\sum_{t=1}^T f(\omega_t; \zeta_t) - \min_{\omega \in \Omega} \sum_{t=1}^T f(\omega; \zeta_t) \leq \frac{\hbar_1 \sqrt{T} + \hbar_2 \ln T + 2\hbar_2}{2\mu \mathcal{D}^{2\theta-1} \delta}. \quad (10)$$

2. When $\theta \in (1/2, 1)$, the expected regret satisfies the inequality:

$$\mathbb{E}_{\zeta_{1:T}} \left[\sum_{t=1}^T f(\omega_t; \zeta_t) \right] - \min_{\omega \in \Omega} \mathbb{E}_{\zeta_{1:T}} \left[\sum_{t=1}^T f(\omega; \zeta_t) \right] \leq T^{1-\frac{1}{4\theta}} \left[\left(\frac{\hbar_1}{2\mu} \right)^{\frac{1}{2\theta}} + 2 \left(\frac{\hbar_2}{2\mu} \right)^{\frac{1}{2\theta}} \right], \quad (11)$$

In addition, let $\delta \in (0, 1)$, then the following inequality on the online regret holds with probability $1 - \delta$:

$$\sum_{t=1}^T f(\omega_t; \zeta_t) - \min_{\omega \in \Omega} \sum_{t=1}^T f(\omega; \zeta_t) \leq \frac{T^{1-\frac{1}{4\theta}}}{\delta} \left[\left(\frac{\hbar_1}{2\mu} \right)^{\frac{1}{2\theta}} + 2 \left(\frac{\hbar_2}{2\mu} \right)^{\frac{1}{2\theta}} \right]. \quad (12)$$

Proof. 1. For the case $\theta \in (0, 1/2]$, we start with (7) and conclude immediately

$$\mathbb{E}_{\omega_{1:T}} \left[\sum_{t=1}^T \mathbb{E}_{\zeta_t} [f(\omega_t; \zeta_t) - f(\omega^*; \zeta_t) | \omega_t] \right] \leq \frac{1}{2\mu \mathcal{D}^{2\theta-1}} \mathbb{E}_{\omega_{1:T}} \left[\sum_{t=1}^T |\nabla F(\omega_t)|^2 \right],$$

which leads to the following inequality,

$$\mathbb{E}_{\zeta_{1:T}} \left[\sum_{t=1}^T f(\omega_t; \zeta_t) - \sum_{t=1}^T f(\omega; \zeta_t) \right] \leq \frac{\hbar_1 \sqrt{T} + \hbar_2 \ln T + 2\hbar_2}{2\mu \mathcal{D}^{2\theta-1}}, \quad \forall \omega \in \Omega.$$

Then, we have

$$\mathbb{E}_{\zeta_{1:T}} \left[\sum_{t=1}^T f(\omega_t; \zeta_t) \right] - \min_{\omega \in \Omega} \mathbb{E}_{\zeta_{1:T}} \left[\sum_{t=1}^T f(\omega; \zeta_t) \right] \leq \frac{\hbar_1 \sqrt{T} + \hbar_2 \ln T + 2\hbar_2}{2\mu \mathcal{D}^{2\theta-1}},$$

which proves (9). Next, we apply Markov's inequality and obtain the following result:

$$\sum_{t=1}^T f(\omega_t; \zeta_t) - \min_{\omega \in \Omega} \sum_{t=1}^T f(\omega; \zeta_t) \leq \frac{\hbar_1 \sqrt{T} + \hbar_2 \ln T + 2\hbar_2}{2\mu \mathcal{D}^{2\theta-1} \delta},$$

which holds with probability $1 - \delta$. This concludes the proof of the first part of Corollary 2.2.

2. For the case $\theta \in (1/2, 1)$, we reformulate (8) in the following form

$$\frac{1}{T} \sum_{t=1}^T \mathbb{E}_{\zeta_t} [f(\omega_t; \zeta_t) - f(\omega^*; \zeta_t) | \omega_t] \leq \left(\frac{1}{2\mu} \right)^{\frac{1}{2\theta}} \left(\frac{1}{T} \sum_{t=1}^T |\nabla F(\omega_t)|^2 \right)^{\frac{1}{2\theta}}.$$

Then we take expectation on both sides to obtain the following inequality

$$\begin{aligned} \frac{1}{T} \mathbb{E}_{\omega_{1:T}} \left[\sum_{t=1}^T \mathbb{E}_{\zeta_t} [f(\omega_t; \zeta_t) - f(\omega^*; \zeta_t) | \omega_t] \right] \\ \leq \left(\frac{1}{2\mu} \right)^{\frac{1}{2\theta}} \mathbb{E}_{\omega_{1:T}} \left[\left(\frac{1}{T} \sum_{t=1}^T |\nabla F(\omega_t)|^2 \right)^{\frac{1}{2\theta}} \right]. \end{aligned}$$

We apply Jensen's inequality for concave functions to the right-hand side of the above inequality, and conclude

$$\begin{aligned} \mathbb{E}_{\omega_{1:T}} \left[\left(\frac{1}{T} \sum_{t=1}^T |\nabla F(\omega_t)|^2 \right)^{\frac{1}{2\theta}} \right] &\leq \left(\frac{1}{T} \mathbb{E}_{\omega_{1:T}} \left[\sum_{t=1}^T |\nabla F(\omega_t)|^2 \right] \right)^{\frac{1}{2\theta}} \\ &\leq \left(\frac{\hbar_1}{\sqrt{T}} + \frac{\hbar_2 \ln T}{T} + \frac{2\hbar_2}{T} \right)^{\frac{1}{2\theta}} \\ &\leq \left(\frac{\hbar_1}{\sqrt{T}} \right)^{\frac{1}{2\theta}} + \left(\frac{\hbar_2 (\ln T + 2)}{T} \right)^{\frac{1}{2\theta}}, \end{aligned}$$

where the last inequality is guaranteed by the subadditivity of concave functions.

Next, we take the leftmost and rightmost sides of the above inequalities, and for all $\omega \in \Omega$ have

$$\begin{aligned} \mathbb{E}_{\zeta_{1:T}} \left[\sum_{t=1}^T f(\omega_t; \zeta_t) - \sum_{t=1}^T f(\omega; \zeta_t) \right] \\ \leq T^{1-\frac{1}{4\theta}} \left[\left(\frac{\hbar_1}{2\mu} \right)^{\frac{1}{2\theta}} + \left(\frac{\hbar_2}{2\mu} \right)^{\frac{1}{2\theta}} (\ln T + 2)^{\frac{1}{2\theta}} T^{-\frac{1}{4\theta}} \right] \\ \leq T^{1-\frac{1}{4\theta}} \left[\left(\frac{\hbar_1}{2\mu} \right)^{\frac{1}{2\theta}} + 2 \left(\frac{\hbar_2}{2\mu} \right)^{\frac{1}{2\theta}} \right], \end{aligned}$$

where the last inequality is based on the fact that for all $\theta \in (1/2, 1)$ and $T \geq 1$ we have

$$(\ln T + 2)^{\frac{1}{2\theta}} T^{-\frac{1}{4\theta}} \leq 2.$$

Furthermore, we have

$$\begin{aligned} \mathbb{E}_{\zeta_{1:T}} \left[\sum_{t=1}^T f(\omega_t; \zeta_t) \right] - \min_{\omega \in \Omega} \mathbb{E}_{\zeta_{1:T}} \left[\sum_{t=1}^T f(\omega; \zeta_t) \right] \\ \leq T^{1-\frac{1}{4\theta}} \left[\left(\frac{\hbar_1}{2\mu} \right)^{\frac{1}{2\theta}} + 2 \left(\frac{\hbar_2}{2\mu} \right)^{\frac{1}{2\theta}} \right], \end{aligned}$$

which proves (11). By applying Markov's inequality we obtain the following result:

$$\sum_{t=1}^T f(\omega_t; \zeta_t) - \min_{\omega \in \Omega} \sum_{t=1}^T f(\omega; \zeta_t) \leq \frac{T^{1-\frac{1}{4\theta}}}{\delta} \left[\left(\frac{\hbar_1}{2\mu} \right)^{\frac{1}{2\theta}} + 2 \left(\frac{\hbar_2}{2\mu} \right)^{\frac{1}{2\theta}} \right],$$

which holds with probability $1 - \delta$. This concludes the proof of the second part of Corollary 2.2. \square

The results of Corollary 2.2 highlight that when $\theta \in (0, 1/2]$, Algorithm 2 is expected to converge at the standard stochastic rate of $\mathcal{O}(1/\sqrt{T})$ (or equivalently $\mathcal{O}(\sqrt{T})$ regret). In contrast, the regret is upper bounded by $\mathcal{O}(T^{1-1/4\theta})$ when $\theta \in (1/2, 1)$. In both cases, the convergence rates are dimension-independent, and the errors in the gradient estimate contribute a factor of $1/1-\kappa$.

3 Interpretation of Algorithm 2 as Trust-Region Approach

In this section, we will interpret Algorithm 2 from the perspective of a trust-region method. However, we only demonstrate the key steps, while the more detailed derivation is included in Appendix B. For a fixed sample ζ , the loss function $f(\omega; \zeta)$ and the parameterized network $\pi(\omega, y; \zeta)$ will be denoted as $f(\omega)$ and $\pi(\omega)$ for notational convenience. A trust-region method solves the following transformed optimization problem at each step (Yuan, 2015; Martínez, 1994; Sorensen, 1982):

$$\begin{aligned} \min_{d \in \Omega} & f(\omega) + \nabla f(\omega)^T d + \frac{1}{2} d^T \nabla^2 f(\omega) d \\ \text{s.t.} & |d| \leq \Delta, \end{aligned}$$

where Δ denotes the radius of the trust region. Drawing inspiration from this idea, we approximate the loss function locally as follows:

$$\begin{aligned} M(v, \omega) = & f(\omega) + (v - \omega)^T \mathcal{L}^T \nabla_y l(y; \zeta) + \frac{1}{2} (v - \omega)^T \mathcal{L}^T \nabla_y^2 l(y; \zeta) \mathcal{L} (v - \omega) \\ & + \underbrace{\frac{\alpha}{2} \left| \nabla_{\omega} \pi(\omega; \zeta)^T (v - \omega) \right|^2}_{\text{Term 1}} + \underbrace{\frac{\epsilon}{2} |v - \omega|^2}_{\text{Term 2}}, \quad (13) \end{aligned}$$

where

$$\mathcal{L} = \frac{\partial y}{\partial \omega} = \left(\mathbf{I} - \mathcal{G}(u) \frac{\partial \pi(\omega, y; \zeta)}{\partial y} \right)^\dagger \mathcal{G}(u) \frac{\partial \pi(\omega, y; \zeta)}{\partial \omega}.$$

We note that Term 1 and Term 2 are used as penalty terms to ensure that when $v \in \Omega$ deviates from the parameters ω , the value of $M(v, \omega)$ remains strictly greater than that of $f(\omega)$. Furthermore, these terms help prevent drastic changes in the parameters

ω and their corresponding outputs $u = \pi(\omega)$ during each iteration of the resulting iterative scheme. In our setting, we can ensure that the trust region constraint is always satisfied, specifically $|v - \omega| \leq \Delta$, by appropriately adjusting the constant ϵ in (13).

Next, we calculate the closed-form solution of the minimum point of $\mathbb{E}_\zeta [M(v, \omega) | \omega]$ as follows:

$$\omega^* = \omega - \frac{1}{\epsilon} (\Sigma_1 + \alpha \Sigma_2 + \mathbf{I})^{-1} \int \mathcal{L}(\xi)^T \nabla_y l(y; \xi) p_\zeta(\xi) d\xi, \quad (14)$$

where

$$\Sigma_1 = \int \mathcal{L}(\xi)^T \nabla_y^2 l(y; \xi) \mathcal{L}(\xi) p_\zeta(\xi) d\xi, \quad \Sigma_2 = \int \nabla_\omega \pi(\omega; \xi) \nabla_\omega \pi(\omega; \xi)^T p_\zeta(\xi) d\xi,$$

and $\mathbf{I} \in \mathbb{R}^{n_\omega \times n_\omega}$ denotes the identity matrix. Since the trust-region function $M(v, \omega)$ provides only a local approximation of the cost function $f(\omega)$ in the vicinity of the point ω , we adopt the following iterative scheme to guide the parameters ω towards the optimal value:

$$\omega_{t+1} = \omega_t - \frac{1}{\epsilon} (\Sigma_1 + \alpha \Sigma_2 + \mathbf{I})^{-1} \int \mathcal{L}(\xi)^T \nabla_y l(y_t; \xi) p_\zeta(\xi) d\xi, \quad t = 1, \dots, T.$$

In the context of stochastic optimization, where global information is lacking, the matrices Σ_1 and Σ_2 are unavailable. Therefore, we employ the following estimates to respectively replace Σ_1 and Σ_2 for $t = 1, \dots, T$:

$$\Sigma_1^t = \frac{1}{\epsilon t} \sum_{k=1}^t \mathcal{L}_k^T \nabla_y^2 l(y_k; \zeta_k) \mathcal{L}_k, \quad \Sigma_2^t = \frac{1}{\epsilon t} \sum_{k=1}^t \nabla_\omega \pi(\omega_k, y_k; \zeta_k) \nabla_\omega \pi(\omega_k, y_k; \zeta_k)^T,$$

Likewise, we replace the term $\int \mathcal{L}(\xi)^T \nabla_y l(y_t; \xi) p_\zeta(\xi) d\xi$ with the estimate $\mathcal{L}_t^T \nabla_y l(y_t; \zeta_t)$. Finally, we introduce the step size η_t at each iteration and get the following iterative scheme:

$$\omega_{t+1} = \omega_t - \eta_t (\Sigma_1^t + \alpha \Sigma_2^t + \mathbf{I})^{-1} \mathcal{L}_t^T \nabla_y l(y_t; \zeta_t). \quad (15)$$

We note that in (15), the term $\nabla_y l(y_t; \zeta_t)$ can be easily obtained at each iteration by observing the output of the cyber-physical system. Meanwhile, Σ_2^t can be obtained by performing backpropagation at each iteration. Therefore, the only term that is difficult to obtain accurately in Algorithm 2 is the gradient \mathcal{L}_t and the corresponding Σ_1^t . Therefore, we use the approximate gradient $\mathcal{G}(u)$ instead of $\partial \mathcal{G}(s_0, u; \zeta) / \partial u$.

4 Connection to Cyber-Physical Systems and Robotics

In this article, we not only emphasize the importance of convergence analysis but also bridge the gap between theory and practical cyber-physical systems. From the analysis in Section 2 we conclude that as long as the approximate gradient $\mathcal{G}(u_t)$ is accurate enough (as characterized by the error modulus κ) convergence is guaranteed and Algorithm 2 can be directly deployed on a cyber-physical system. We note that for cyber-physical systems, common estimation methods include system identification and finite difference estimation (Ljung, 2010; Pintelon and Schoukens, 2012; Carè et al, 2018; Tsiamis and Pappas, 2019; Campi and Weyer, 2002). In the following examples, we will use these estimation methods to demonstrate the broad applicability and robustness (insensitivity to modeling errors) of our algorithm.

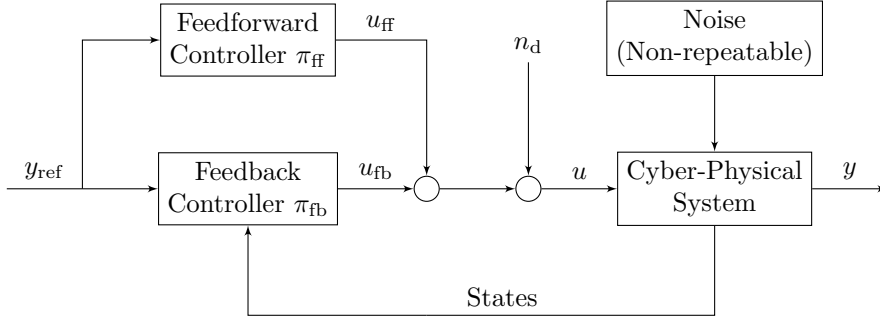
First of all, we endow the random variable ζ with a specific meaning for cyber-physical systems. In the following sections of this article, we consider the random variable ζ as the reference trajectory $y_{\text{ref}} \in \mathcal{Y}^q$ that the system is required to track. Given that the learning task is trajectory tracking, an intuitive choice for the loss function l is the deviation from the reference trajectory, that is,

$$l(y_t; y_{\text{ref},t}) := \frac{1}{2} |G(s_0, u_t; y_{\text{ref},t}) - y_{\text{ref},t}|^2, \quad y_{\text{ref},t} \stackrel{\text{i.i.d.}}{\sim} p_{y_{\text{ref}}}, \quad t = 1, \dots, T. \quad (16)$$

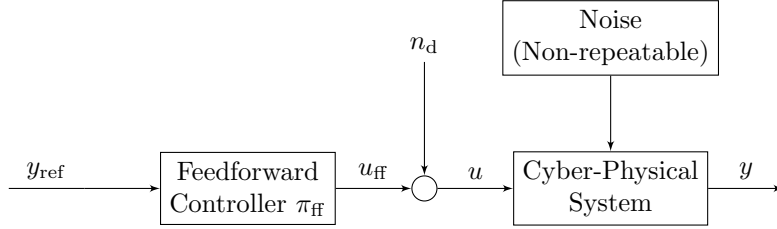
Thereby, we have $\nabla_y^2 l(y; \zeta) = \text{I}$. As delineated in (1), t denotes the current iteration, with the total iterations denoted by T . This notation inherently suggests that the reference trajectory y_{ref} evolves in correspondence with the progression of iterations. Concurrently, at each iteration, the reference trajectory is randomly sampled from a fixed yet unknown distribution $p_{y_{\text{ref}}}$. The distribution $p_{y_{\text{ref}}}$ depends upon the specific robotic task at hand, with trajectory tracking serving as a broad, universal objective. For example, in the context of training a robot for table tennis, $p_{y_{\text{ref}}}$ is determined by the trajectories experienced by the end-effector during ball interception (Ma et al, 2022, 2023; Tobuschat et al, 2023). Given the specific meaning of ζ and the action parameterization π , implies that we have identified a nonlinear feedforward and feedback controller that yields accurate trajectory tracking for any $y_{\text{ref}} \sim p_{y_{\text{ref}}}$ when solving (3). For simplification and without really compromising generality (we could extend the function π to also account for s_0), we assume that the system consistently initializes from an identical state prior to each iteration. As such, the initial state s_0 can be fixed and omitted. For example, in the experiments with the ping-pong robot we drive the robot back to a rest position after each iteration of the online learning with a simple proportional-integral-derivative (PID) controller.

To address the learning tasks in cyber-physical systems, we draw inspiration from the classical two-degrees-of-freedom control framework, which includes a feedforward block and a feedback block, and is shown in Figure 2a. The two-degrees-of-freedom control loop has extensive applications in machine learning within the context of robotics. We can contrast our approach of learning feedforward and feedback controllers to RL, where the objective is to learn a feedback controller (policy) that

minimizes a designated reward function (Sutton and Barto, 2018; Li, 2018). In contrast to RL, which is often based on approximately solving the Bellman equation, we do not use any dynamic programming strategy in our approach.



(a) two-degrees-of-freedom control loop



(b) feedforward control loop

Fig. 2: The figure shows the classical two-degrees-of-freedom control framework in panel (a), which includes a feedforward controller and a feedback controller, and a pure feedforward control framework in panel (b). The variable n_d denotes a disturbance, which will subsequently be used to obtain an approximate gradient $\mathcal{G}(u_t)$.

In our approach, we use π_{ff} and π_{fb} to represent the parameterized feedforward and feedback networks, respectively, and ω_{ff} and ω_{fb} to denote their corresponding parameters. Then, the relation between y_t and u_t in (3) can be reformulated as follows:

$$\begin{aligned} y_t &= G(s_0, u_t; \zeta_t), \\ u_t &= \pi_{\text{ff}}(\omega_{\text{ff},t}; \zeta_t) + \pi_{\text{fb}}(\omega_{\text{fb},t}; y_t - \zeta_t), \quad \zeta_t \stackrel{\text{i.i.d.}}{\sim} p_{\zeta}, \end{aligned} \tag{17}$$

that is, the input u_t is the combination of a feedforward part π_{ff} that does not depend on y_t and a feedback part π_{fb} that depends on the deviation of y_t from the reference trajectory ζ_t . Due to the inclusion of feedback π_{fb} , the calculation of the gradient in Algorithm 2 becomes more complex and less intuitive compared to the open-loop situation where $\pi_{\text{fb}} = 0$. Hence, we will demonstrate the computation of the gradients

$\partial y/\partial\omega_{\text{ff}}$ and $\partial y/\partial\omega_{\text{fb}}$ in the closed-loop system and discuss their implications. The critical aspect to note at this point is that (17) defines an implicit equation for y_t and also u_t . We should therefore think of y_t and u_t as functions of ω_{ff} , ω_{fb} and ζ_t , that is, $u = u(\omega_{\text{ff}}, \omega_{\text{fb}}; \zeta)$ and $y = y(\omega_{\text{ff}}, \omega_{\text{fb}}; \zeta)$. The gradient of the loss function f with respect to the parameters can be calculated as follows:

$$\nabla_{\omega} f(\omega; \zeta) = \begin{bmatrix} \frac{\partial y^{\text{T}}}{\partial\omega_{\text{ff}}} & \frac{\partial y^{\text{T}}}{\partial\omega_{\text{fb}}} \end{bmatrix} \nabla_y l(y; \zeta).$$

By combining the two equations in (17) we get a single implicit equation for y . The differential $\partial y/\partial\omega_{\text{ff}}$ can now be obtained by differentiating the implicit equation with respect to ω_{ff} (implicit function theorem):

$$\frac{\partial y}{\partial\omega_{\text{ff}}} = \frac{\partial G(u; \zeta)}{\partial u} \Big|_{u=\pi_{\text{ff}}+\pi_{\text{fb}}} \frac{\partial \pi_{\text{fb}}(\omega_{\text{fb}}; \zeta^{\circ})}{\partial \zeta^{\circ}} \Big|_{\zeta^{\circ}=G(u; \zeta)-\zeta} \frac{\partial y}{\partial\omega_{\text{ff}}} + \frac{\partial G(u; \zeta)}{\partial u} \Big|_{u=\pi_{\text{ff}}+\pi_{\text{fb}}} \frac{\partial \pi_{\text{ff}}(\omega_{\text{ff}}; \zeta)}{\partial \omega_{\text{ff}}}.$$

This can be rearranged to

$$\frac{\partial y}{\partial\omega_{\text{ff}}} = \left(\mathbf{I} - \frac{\partial G(u; \zeta)}{\partial u} \frac{\partial \pi_{\text{fb}}(\omega_{\text{fb}}; \zeta^{\circ})}{\partial \zeta^{\circ}} \Big|_{\zeta^{\circ}=G(u; \zeta)-\zeta} \right)^{\dagger} \frac{\partial G(u; \zeta)}{\partial u} \frac{\partial \pi_{\text{ff}}(\omega_{\text{ff}}; \zeta)}{\partial \omega_{\text{ff}}}. \quad (18)$$

The expression $\partial y/\partial\omega_{\text{fb}}$ can be derived with a similar argument and results in

$$\frac{\partial y}{\partial\omega_{\text{fb}}} = \left(\mathbf{I} - \frac{\partial G(u; \zeta)}{\partial u} \frac{\partial \pi_{\text{fb}}(\omega_{\text{fb}}; \zeta^{\circ})}{\partial \zeta^{\circ}} \Big|_{\zeta^{\circ}=G(u; \zeta)-\zeta} \right)^{\dagger} \frac{\partial G(u; \zeta)}{\partial u} \frac{\partial \pi_{\text{fb}}(\omega_{\text{fb}}; \zeta^{\circ})}{\partial \omega_{\text{fb}}} \Big|_{\zeta^{\circ}=G(u; \zeta)-\zeta}. \quad (19)$$

We observe that the term $\partial G(u; \zeta)/\partial u$ consistently represents the gradient of the open-loop system and, as previously mentioned, can be approximated using the estimate $\mathcal{G}(u)$. This approximation renders the terms $\partial y/\partial\omega_{\text{ff}}$ and $\partial y/\partial\omega_{\text{fb}}$ computable. We also note that the feedback controller may reduce the effect of estimation errors in \mathcal{G} on the resulting gradient estimates \mathcal{F} . Indeed, if $\partial \pi_{\text{fb}}(\omega_{\text{fb}}; \zeta^{\circ})/\partial \zeta^{\circ}$ is large, both expressions reduce to

$$\frac{\partial \pi_{\text{fb}}(\omega_{\text{fb}}; \zeta^{\circ})^{\dagger}}{\partial \zeta^{\circ}} \frac{\partial \pi_{\text{fb}}(\omega_{\text{fb}}; \zeta^{\circ})}{\partial \omega_{\text{fb}}}, \quad \frac{\partial \pi_{\text{fb}}(\omega_{\text{fb}}; \zeta^{\circ})^{\dagger}}{\partial \zeta^{\circ}} \frac{\partial \pi_{\text{ff}}(\omega_{\text{ff}}; \zeta)}{\partial \omega_{\text{ff}}},$$

respectively, which means that ∇f is approximately independent of G for large $\partial\pi_{\text{fb}}(\omega_{\text{fb}}; \zeta^\circ)/\partial\zeta^\circ$. If the feedback gain is small, however, $\partial y/\partial\omega_{\text{ff}}$ and $\partial y/\partial\omega_{\text{fb}}$ reduce to

$$\frac{\partial G(s_0, u; \zeta)}{\partial u} \frac{\pi_{\text{ff}}(\omega_{\text{ff}}; \zeta)}{\partial\omega_{\text{ff}}}, \quad \frac{\partial G(s_0, u; \zeta)}{\partial u} \frac{\pi_{\text{fb}}(\omega_{\text{fb}}; \zeta^\circ)}{\partial\omega_{\text{fb}}}.$$

Moving forward, we will briefly show that the term

$$\left(\mathbf{I} - \frac{\partial G(u; \zeta)}{\partial u} \frac{\partial\pi_{\text{fb}}(\omega_{\text{fb}}; \zeta^\circ)}{\partial\zeta^\circ} \right)^\dagger \frac{\partial G(u; \zeta)}{\partial u} \quad (20)$$

is the gradient of the closed-loop system with respect to the external input n_{d} (see Figure 2). This finding enables us to directly derive gradient estimation approaches for the closed-loop system, which will be denoted as $\mathcal{G}^\circ(\omega_{\text{ff}}, \omega_{\text{fb}}, \zeta)$. We perform the following calculations (implicit function theorem):

$$\frac{\partial y}{\partial n_{\text{d}}} = \frac{\partial G(u; \zeta)}{\partial u} \Big|_{u=\pi_{\text{ff}}+\pi_{\text{fb}}} \frac{\partial\pi_{\text{fb}}(\omega_{\text{fb}}; \zeta^\circ)}{\partial\zeta^\circ} \Big|_{\zeta^\circ=G(u; \zeta)-\zeta} \frac{\partial y}{\partial n_{\text{d}}} + \frac{\partial G(u; \zeta)}{\partial u} \Big|_{u=\pi_{\text{ff}}+\pi_{\text{fb}}},$$

which results in

$$\frac{\partial y}{\partial n_{\text{d}}} = \left(\mathbf{I} - \frac{\partial G(u; \zeta)}{\partial u} \frac{\partial\pi_{\text{fb}}(\omega_{\text{fb}}; \zeta^\circ)}{\partial\zeta^\circ} \right)^\dagger \frac{\partial G(u; \zeta)}{\partial u}.$$

Intuitively, $\partial y/\partial n_{\text{d}}$ describes the sensitivity of y in closed-loop to changes in u .

Consequently, the terms $\partial y/\partial\omega_{\text{ff}}$ and $\partial y/\partial\omega_{\text{fb}}$, apart from being derived from (18) and (19), can also be obtained through the following more direct approach

$$\frac{\partial y}{\partial\omega_{\text{ff}}} = \mathcal{G}^\circ(\omega_{\text{ff}}, \omega_{\text{fb}}, \zeta) \frac{\partial\pi_{\text{ff}}(\omega_{\text{ff}}; \zeta)}{\partial\omega_{\text{ff}}}, \quad \frac{\partial y}{\partial\omega_{\text{fb}}} = \mathcal{G}^\circ(\omega_{\text{ff}}, \omega_{\text{fb}}, \zeta) \frac{\partial\pi_{\text{fb}}(\omega_{\text{fb}}; \zeta^\circ)}{\partial\omega_{\text{fb}}},$$

thereby allowing for direct computations if \mathcal{G}° is known. As we will highlight with simulation experiments $\mathcal{G}^\circ(\omega_{\text{ff}}, \omega_{\text{fb}}, \zeta)$ can be computed directly by performing stochastic rollouts with different random perturbations n_{d} (see Section 5.2).

5 Experiments

In this section, we will demonstrate the effectiveness of our algorithms through extensive experiments conducted on various cyber-physical systems, including simulation and real-world experiments. Additionally, we evaluate the accuracy of the theoretical convergence rate of the algorithm proposed in Section 2. In each experiment, we will first introduce the underlying cyber-physical system. Then, based on the specific systems, we will describe the distribution of the reference trajectories, the structure of the

parameterized models π , and the corresponding structure of the inputs. We highlight that even shallow networks work well with our algorithms. Depending on different scenarios, we will employ an appropriate method to obtain gradient estimates $\mathcal{G}(u)$ and \mathcal{G}° . Finally, we will discuss the results of the experiments in terms of convergence rate and robustness to modeling errors. It is worth mentioning that the primary intention of the following experiments is not to outperform any existing (reinforcement) learning algorithms but to evaluate the effectiveness of our algorithms and offer another possibility for the development of machine learning in the field of robotics.

5.1 Cantilever Beam

The first example is based on the control of a flexible cantilever beam. The example illustrates how our approach can easily handle dynamical systems with a large number of hidden states (here 100). We note that current RL algorithms have difficulties in dealing with continuous state and action spaces exceeding two dozen states. Modeling and controlling flexible structures has numerous engineering applications (Shabana, 1997; Amirouche, 2007), such as active vibration control of wind turbines, aircraft wings or turbo generator shafts. We consider a cantilever beam illustrated in Figure 3, where the left end of the beam is hinged to a joint, and the active torque τ is applied only at the left end to counteract the disturbances at the tip of the flexible body. The total length of the entire cantilever beam in a rest configuration is denoted by l .

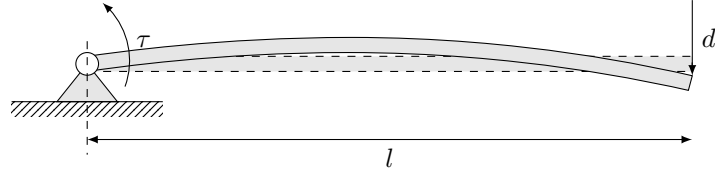


Fig. 3: Deformation of the cantilever beam under the active torque and an external disturbance d , where the dashed line represents the position of the cantilever beam when at rest.

We employ a lumped-parameter method to discretize the cantilever beam, as illustrated in Figure 4, into a collection of n rigid units. In the discrete model of the cantilever beam, the entire beam is divided into n rigid units, either uniformly or non-uniformly. These rigid units are coupled through joints equipped with internal springs and dampers. The joints provide the degrees of freedom required for deformation. The mass, spring, and damper elements offer inertial, restorative, and dissipative forces, respectively, which collectively account for the deformation. Typically, due to the small deformation assumption, the springs and dampers inside each joint are considered linear. In this experiment, however, we will explore the performance of our algorithms in nonlinear systems. Therefore, we adjust the parameters of the cantilever beam (such as the moment of inertia and damping parameters) to enable large deformations and

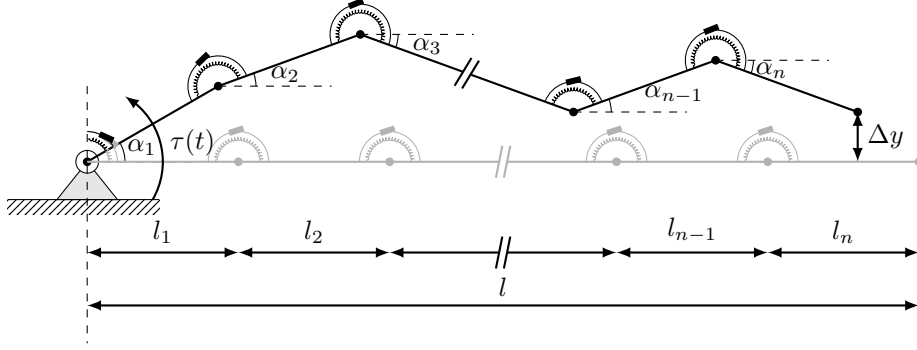


Fig. 4: The figure depicts the discrete model of the cantilever beam obtained using the lumped-parameter method. The entire beam is decomposed into n rigid units, with adjacent units interconnected by a pair of spring and damper. Each rigid unit has a length of l_i , and the angle it makes with the horizontal plane is denoted by α_i . The active torque is applied only to the first rigid unit hinged to the wall. The gray object indicates the position of the beam when at rest.

introduce the following nonlinear spring force:

$$f_{\text{spring},i}(\Delta\alpha_i) = k_{i1}\Delta\alpha_i + k_{i2}\Delta\alpha_i^3 + k_{i3}\Delta\alpha_i^5, \quad i = 1, \dots, n,$$

where $\Delta\alpha_i := \alpha_i - \alpha_{i-1}$ represents the angular difference between two adjacent rigid units, and $\alpha_0 = 0$. The sole active torque is applied to the first rigid unit. All specific parameters used in this experiment are summarized in Table 3. The following experiments are implemented in `Matlab` and `Simulink`.

Table 3: Parameters of the discrete beam model.

Parameter	Value	Unit	Description
n	50	-	number of rigid units
l_i	3×10^{-2}	m	length of each rigid unit
I_A	5×10^{-3}	m^4	the moment of inertia
k_{i1}	5	N m/rad	spring coefficient
k_{i2}	1×10^3	N m/rad^3	spring coefficient
k_{i3}	1×10^4	N m/rad^5	spring coefficient
b_i	30	N s/rad	damper coefficient

5.1.1 Reference Trajectory Distribution

The aim of this experiment is to utilize Algorithm 2 to learn the parameterized networks π_{ff} and π_{fb} in an online manner (see Figure 2). The outputs of the parameterized networks yield the active torque τ . The aim of the online learning is to find the parameters ω_{ff} and ω_{fb} , in order to minimize the tracking error of the end-effector ($|y - y_{\text{ref}}|$)

for reference trajectories sampled from the unknown distribution $p_{y_{\text{ref}}}$. The output y describes the distance in y -direction between the tip of the beam and the horizontal plane. We observe that the presence of nonlinear spring forces and large deformations, coupled with as many as 100 hidden states (position and velocity in y -direction of each unit), renders this task highly challenging.

All reference trajectories used in the experiment arise from sampling an unknown but fixed distribution. At each iteration, we randomly generate the reference trajectory based on the following principles: 1. Over a time span of T_{sim} seconds, the trajectory starts from rest and eventually returns to its initial position, and remains still for an additional 0.5 s. 2. Apart from the starting and ending points (y_0 and y_T), two other time points, t_a and t_b , will be randomly selected within the time duration T_{sim} . The displacements (y_a and y_b) and velocities (v_a and v_b) at these moments will also be randomly generated, with the accelerations being set to zero. 3. The four points are connected using trajectories that minimize jerk³ (Geering, 2007; Piazzoli and Visioli, 1997). The values of the various parameters are summarized in Table 4.

Table 4: Summary of the parameters used for generating reference trajectories.

Parameter	Distribution	Unit
t_a	Uniform(1.2, 1.8)	s
t_b	Uniform(2.9, 3.5)	s
y_a, y_b	Uniform(-0.2, 0.2)	m
v_a, v_b	Uniform(-2.0, 2.0)	m/s

Figure 5 illustrates the sampling procedure for the reference trajectories along with 400 samples. The total duration is set to $T_{\text{sim}} = 5.5$ s. The red dashed boxes indicate the spatial and temporal distribution range of the points y_a and y_b , respectively. We observe that the range of the trajectory is extensive and is not limited to small deformations. In the subsequent experiments, we will see that the parameterized networks trained by our algorithms effectively generalize well across the entire support of $p_{y_{\text{ref}}}$.

5.1.2 Gradient Estimation

As mentioned in Section 3, most of the terms required by Algorithm 2 can be obtained through measurement and computation. However, since the system G is treated as a black-box model, the gradient of the system $\partial G(s_0, u; \zeta) / \partial u$ cannot be analytically determined. To address this, in this numerical experiment, we employ system identification in the frequency domain to obtain a rough linear estimate of $\partial G(s_0, u; \zeta) / \partial u$ (Pintelon and Schoukens, 2012). We excite the discrete model in Simulink with an excitation signal ranging from 0 Hz to 4 Hz, with an interval of 0.1 Hz. The resulting system response in the frequency domain and the estimated linear transfer function are shown in Figure 6. Next, we use the obtained transfer function to construct a linear approximation of $\partial G(s_0, u; \zeta) / \partial u$, which is denoted by \mathcal{G} . It is important to emphasize that in

³Jerk is defined as the derivative of acceleration of the third derivative of displacement.

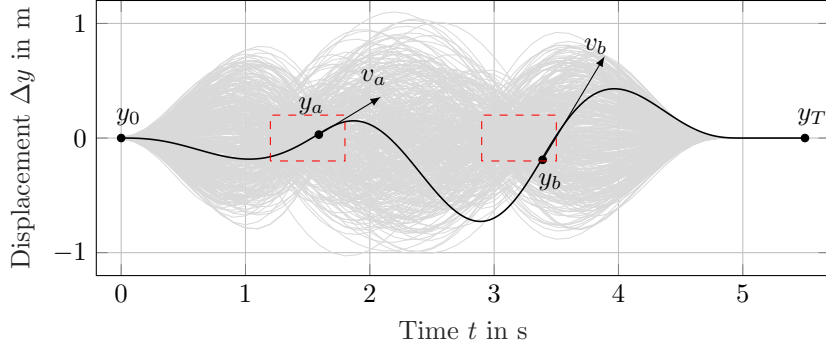


Fig. 5: The figure illustrates the range of reference trajectories used for training, where the gray lines are composed of 400 randomly sampled reference trajectories. The red dashed boxes indicate the spatial and temporal distribution range of the points y_a and y_b , respectively.

this case the gradient estimate \mathcal{G} is static, meaning that it does not change as a function of u . For the specific construction method, please refer to [Ma et al \(2022, 2023\)](#). We observe that the system exhibits a high degree of nonlinearity, which is reflected by the fact that the uncertainty (residual of the linear model) is dominated by the nonlinearities $\sigma_{\text{nonlinear}}$.

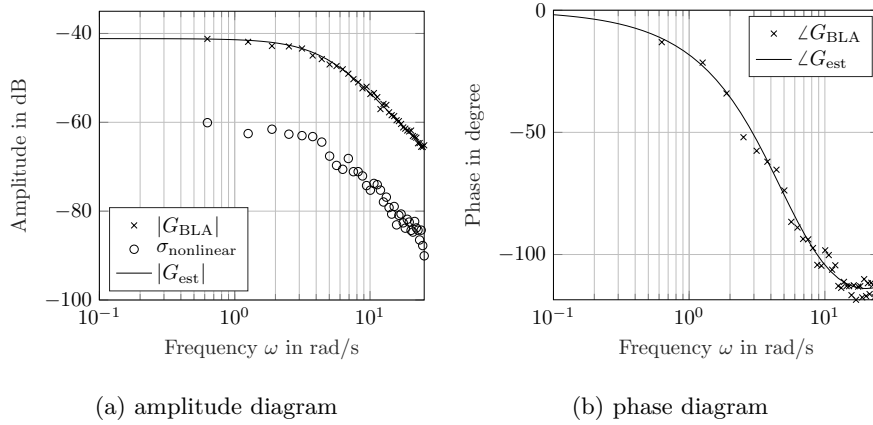


Fig. 6: The figure displays the amplitude diagram (left) and phase diagram (right) of the system response in the frequency domain. Crosses represent the measured data obtained through system identification in frequency domain, while the solid line represents the fitted transfer function. The nonlinearity system is denoted by circles in the amplitude diagram.

Additionally, we estimate the closed-loop system gradient $\mathcal{G}^\circ(\omega_{\text{ff}}, \omega_{\text{fb}}, \zeta)$ using (20):

$$\mathcal{G}^\circ(\omega_{\text{ff}}, \omega_{\text{fb}}, \zeta) = \left(\mathbf{I} - \mathcal{G} \frac{\partial \pi_{\text{fb}}(\omega_{\text{fb}}; \zeta^\circ)}{\partial \zeta^\circ} \right)^\dagger \mathcal{G}.$$

5.1.3 Network and Input Structure

As mentioned in Section 4, each iteration necessitates the cyber-physical system to track a distinct reference trajectory. This means that the parameterized network π , particularly the feedforward network π_{ff} , must be able to adapt to reference trajectories of different lengths. The situation in the case of the beam experiment is illustrated in Figure 7. The policy network π_{ff} takes in a horizon of h_1 steps in the past and h_2 steps in the future to produce the input $u_{k,\text{ff}}$ at time k (see Figure 7a), while π_{fb} takes only h_1 steps in the past to produce $u_{k,\text{fb}}$ (see Figure 7b). In instances where the horizon surpasses the range of the reference trajectory, we employ a zero-padding strategy to compensate for the absent elements.

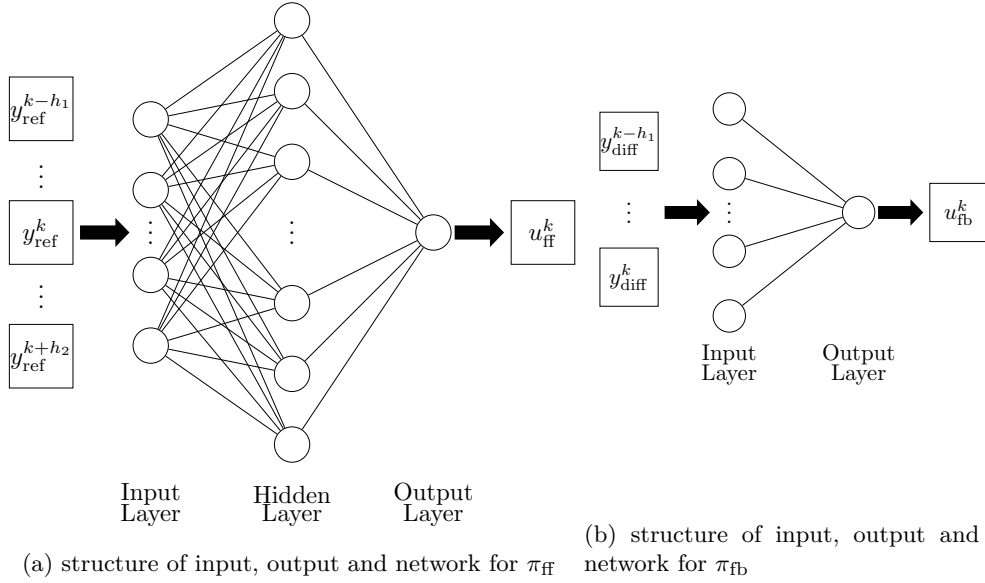


Fig. 7: The figure illustrates the input, output, and network structures of both π_{ff} and π_{fb} . The feedforward network π_{ff} , which is a fully connected network, utilizes the reference trajectory at time k , as well as the reference trajectories for the horizons of h_1 and h_2 before and after this time, as its input. The output is the corresponding feedforward input $u_{k,\text{ff}}$ at time k . On the other hand, the feedback network π_{fb} , a linear network, employs the trajectory difference for a horizon of h_1 units leading up to time k as its input. The output is the respective feedback input $u_{k,\text{fb}}$ at time k . The trajectory difference is defined as the difference between the output trajectory and the reference trajectory.

5.1.4 Experiments

In this section, we employ two strategies to parameterize the feedforward network π_{ff} . One is a linear network, denoted as π_{ff}^1 . The other is a nonlinear network, represented by π_{ff}^2 , which is a fully-connected network with a single hidden layer. The ReLU function is used as the activation function for the hidden layer, and no activation function is applied to the output layer. We consistently use a linear feedback network π_{fb} , and considering the causality of the system, the feedback network only contains the historical information, implying that $h_2 = 0$.

The overview of different experiments is presented in Table 5. In a noise-free environment, trajectory tracking can be viewed as a purely feedforward control task. Therefore, in Experiments 1-4, we employ only the feedforward network π_{ff} and adjust the parameter ϵ , allowing Algorithm 2 to transition between gradient descent ($\epsilon \rightarrow \infty$) and the quasi-Newton method. Through these experiments, we explore the convergence rates of different networks and investigate the influence of different algorithms on convergence as well as their robustness to the selection of hyper-parameters. Subsequently, we intentionally introduce noise n_d to the inputs of the system (see Figure 2a), rendering the pure feedforward network ineffective for the task at hand (see Experiment 5). Experiment 6 demonstrates the ability of the combined feedforward and feedback control (π_{ff} and π_{fb}) to resist noise in online learning.

Table 5: Overview of parameters, network configurations, and experimental results.

No.	Model(s)	h_1	h_2	Hidden Neurons	Noise	ϵ	α	η	Average Loss
1	π_{ff}^1	100	100	-	no	$+\infty$	-	0.1	6.90×10^{-3}
2	π_{ff}^1	100	100	-	no	1.0	0.1	15.0	6.30×10^{-3}
3	π_{ff}^2	100	100	40	no	$+\infty$	-	0.1	8.27×10^{-4}
4	π_{ff}^2	100	100	40	no	1.0	0.1	15.0	3.19×10^{-4}
5	π_{ff}^2	100	100	40	yes	1.0	0.1	15.0	1.10×10^{-3}
6	π_{fb} π_{ff}^2	25 100	- 100	- 40	yes	1.0	0.1	15.0	4.65×10^{-4}

In each experiment, we train the parameterized networks for 1000 iterations. The average loss δ_t is given by

$$\delta_t = \frac{1}{t} \sum_{k=1}^t l(y_k; y_{\text{ref},k}), \quad t = 1, \dots, T.$$

The convergence results of Experiments 1 and 3 are illustrated in Figure 8a, while the results of Experiments 2 and 4 are shown in Figure 8b. We note that, limited by

the complexity of the model, the convergence results of nonlinear models are significantly better than those of linear models, regardless of whether the gradient descent algorithm or the quasi-Newton method is used. At the same time, we also notice that, under the premise of using nonlinear models, the convergence results of the quasi-Newton method are superior to those of the gradient descent algorithm. We believe that this is due to Term 2 in (B10), which is used to capture the local curvature of the loss functions, and the absence of Term 1 in (B10), leading to a lack of constraint on the changes in the outputs of π_{ff} and π_{fb} . In our experiments, such a constraint is important for our online learning tasks, ensuring that the outputs between iterations do not change drastically, thereby preventing oscillations. Moreover, the quasi-Newton method demonstrates greater robustness in the adjustment of hyperparameters, such as the step size η , which requires additional fine-tuning for the gradient descent algorithm.

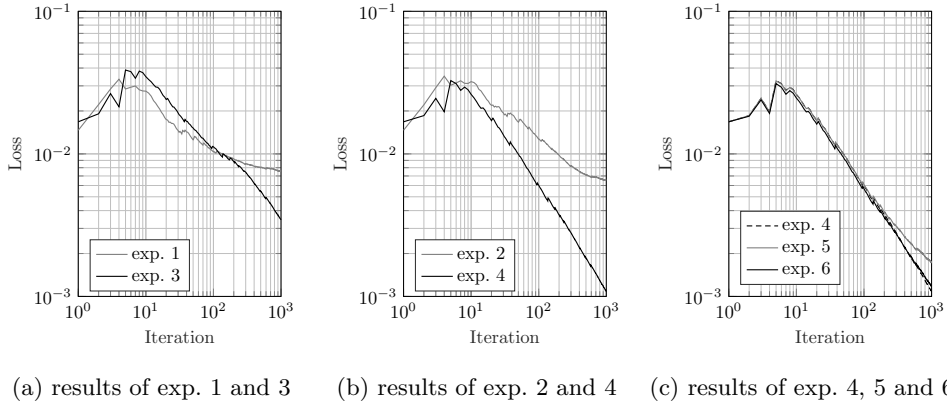


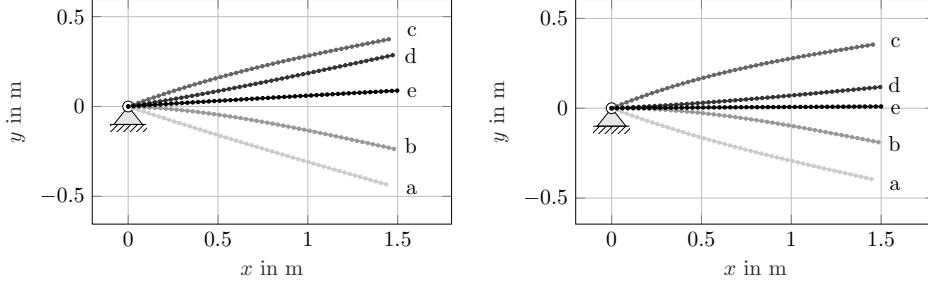
Fig. 8: This figure depicts the convergence results δ_t , $t = 1, \dots, 1000$ of different experiments.

In Experiment 5, we artificially introduce noise n_d to render the purely feedforward control ineffective in trajectory tracking and introduce a feedback controller in Experiment 6 to reject noise, with the convergence results shown in Figure 8c. The introduction of the feedback controller successfully rejects the process noise.

Additionally, we evaluate the performance of all the obtained parameterized networks trained in different experiments on a newly generated test data set previously unseen by our algorithms (see the average loss in Table 5), in order to investigate the generalization capability of the networks. Although we only utilize a linear static gradient estimate \mathcal{G} (which, unsurprisingly, is a very poor estimate), the algorithms still perform well using either gradient descent method or quasi-Newton method, reflecting its strong robustness to modeling errors.

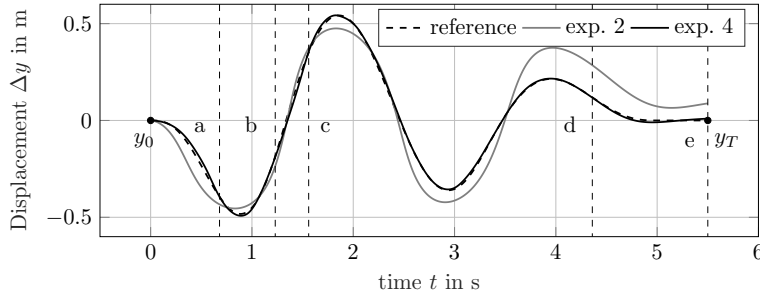
Lastly, we select a trajectory from the test data set to demonstrate the tracking performance of the models obtained in Experiments 2 and 4. The upper subfigure of Figure 9 shows the positions of the beam controlled by the linear and nonlinear

models at different selected moments. The lower subfigure illustrates the tracking error of the beam tip in the y -direction as controlled by the different models.



(a) motion of the beam in exp. 2

(b) motion of the beam in exp. 4



(c) motion of the tip in y -direction

Fig. 9: This figure shows the overall motion of the beam (upper) and the motion of the tip in the y -direction (lower) when the models obtained in Experiments 2 and 4 track the reference trajectory from test data set. The motion starts from a standstill and proceeds in the order of a-b-c-d-e, with the corresponding moments marked with the same labels in the lower subfigure.

5.1.5 Benchmarks with other Approaches

We compare the performance of several algorithms from Section 1.3 with our proposed methods in this experiment. The results are shown in Figure 10. Specifically, the Robust Adaptive Control (RAC) algorithm is based on the work of Dean et al (2018), the Adversarial Control via System Identification (ACSI) algorithm is based on the work of Hazan et al (2020); Agarwal et al (2019), and the Online Non-Stochastic Control (ONSC) algorithm is based on the work of Yan et al (2023) where the different subscripts indicate the number of random perturbations used for estimating the linear model. Figure 10a illustrates the performance of different algorithms on the same

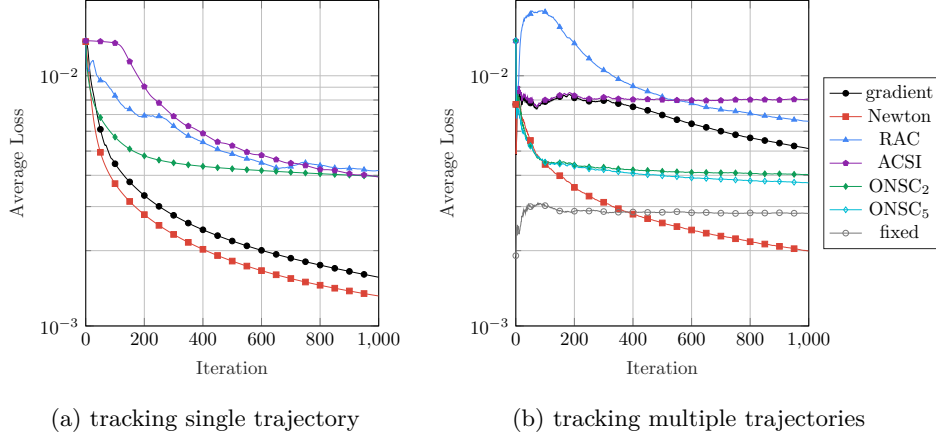


Fig. 10: The figure presents the trajectory tracking results of different algorithms. The left plot depicts tracking performance for a single fixed trajectory, whereas the right plot shows the performance across multiple randomly sampled trajectories.

fixed trajectory. We observe that all algorithms eventually converge, but our methods exhibit both faster convergence rates and better final performance. Figure 10b shows the performance under a fixed number of experiments. We find that only our quasi-Newton method outperforms the fixed best linear controller. The ACSI algorithm does not adapt well to this setting and shows no signs of convergence. For the ONSC algorithm, increasing the number of perturbations used for model estimation slightly improves performance, but also significantly increases computational complexity.

5.2 Four-Legged Robot

In this simulation, we adopt the ant model (Schulman et al, 2018) frequently used to demonstrate RL algorithms to evaluate the effectiveness of our algorithms. The ant model is a quadruped robot with four legs symmetrically distributed around the torso, each connected by two hinged joints, providing two degrees of rotational freedom per leg and eight degrees in total for the ant. In our simulation environment, we have chosen Isaac Gym (Makoviychuk et al, 2021) for its ability to support large-scale parallel simulations, which enables us to rapidly estimate system gradients using a stochastic finite difference method. It is important to emphasize that the traditional RL task on this model focuses on enabling the ant to move forward as quickly as possible. However, in our experiment, our aim is to enable the ant to track any reference trajectory of the center of the mass of the torso. It should be noted that in this experiment, we do not artificially introduce system noise, thus the trajectory tracking task can be considered a purely feedforward control task. Therefore, we only employ a feedforward model π_{ff} , which implies that $\pi_{\text{fb}} = 0$.

We recognize that the learning of the motion of the ant, without any prior knowledge, is a challenging task. Compared to the numerical examples mentioned

in Section 5.1, the learning of the motion present the following differences and difficulties: First, due to the contacts and interactions between the ant and the environment, the motion of the ant is non-smooth, and accordingly, its gradients are discontinuous (though still assumed to be bounded). Second, the states of the ant are not fully observable. In fact, in this experiment only the information about the torso is assumed to be measurable and observable, including its positions, orientations, and corresponding velocities and angular velocities. This means that changes in control inputs do not necessarily cause changes in the outputs. For instance, when one of the legs is not in contact with the ground, the positional change of this leg caused by input variation will not affect the posture of the torso. Third, walking, as a periodic behavior, should follow specific gaits and frequencies. Training a network model from scratch may lead to the ant exhibiting anomalous behaviors.

To overcome the challenges mentioned above, we make the following adjustments to the networks in this experiment:

1. We input the entire reference trajectory for $k = 0$ to $k = T_{\text{sim}}$ into the model and predict the entire control sequence for $k = 0$ to $k = T_{\text{sim}}$.
2. We fix the duration of the trajectory, but we can still adapt the networks to varying trajectory lengths through appropriate preprocessing.
3. We use a pre-trained linear model to provide prior knowledge of ant motion patterns.

5.2.1 Reference Trajectory Distribution

In this experiment, we can only measure and observe the information about the torso, which includes the position of the torso, its orientation represented by a quaternion, and the translational and angular velocities of the torso. The ant moves on a rough and infinitely flat plane, therefore the reference trajectories contain only three components: the planar position of the torso, i.e., the x and y coordinates, and the yaw, which is the rotation of the torso around the z -axis.

Figure 11 displays the distribution of the reference trajectories used for tracking. We take one of the sampled trajectories as an example to illustrate the general rules for generating reference trajectories. The trajectories are generated over a time duration of $T_{\text{sim}} = 4$ s. The starting point p_0 is fixed at the point $[0, 0]^T$ in the x - y plane at time $t_0 = 0$ s, and the initial velocity v_0 is also fixed at 1 m s^{-1} directed along the positive x -axis. Next, we uniformly generate the point p_1 within a disk centered around p_0 with radii of 2 m and 2.5 m, and an angular span of $\pm 60^\circ$ centered around v_0 (see the red dashed disk in the left subfigure). The velocity v_1 at p_1 is also set to 1 m s^{-1} , in the direction of the line from p_0 to p_1 . The time t_1 for generating p_1 is uniformly within a range of ± 0.3 s centered around $t = 2$ s (see the shadow areas in the right subfigures). Based on the point p_1 , the point p_2 and its corresponding velocity v_2 are generated in the same manner, with the time point $t_2 = 4$ s being fixed for p_2 . The acceleration at each point is set to zero. Finally, we connect these three points using a trajectory that minimizes jerk. We note that the duration of all trajectories is fixed. However, since the time duration T_{sim} is sufficiently long to accommodate multiple gaits, trajectories with varying durations can still be accommodated simply by periodically reapplying π_{ff} and π_{fb} .

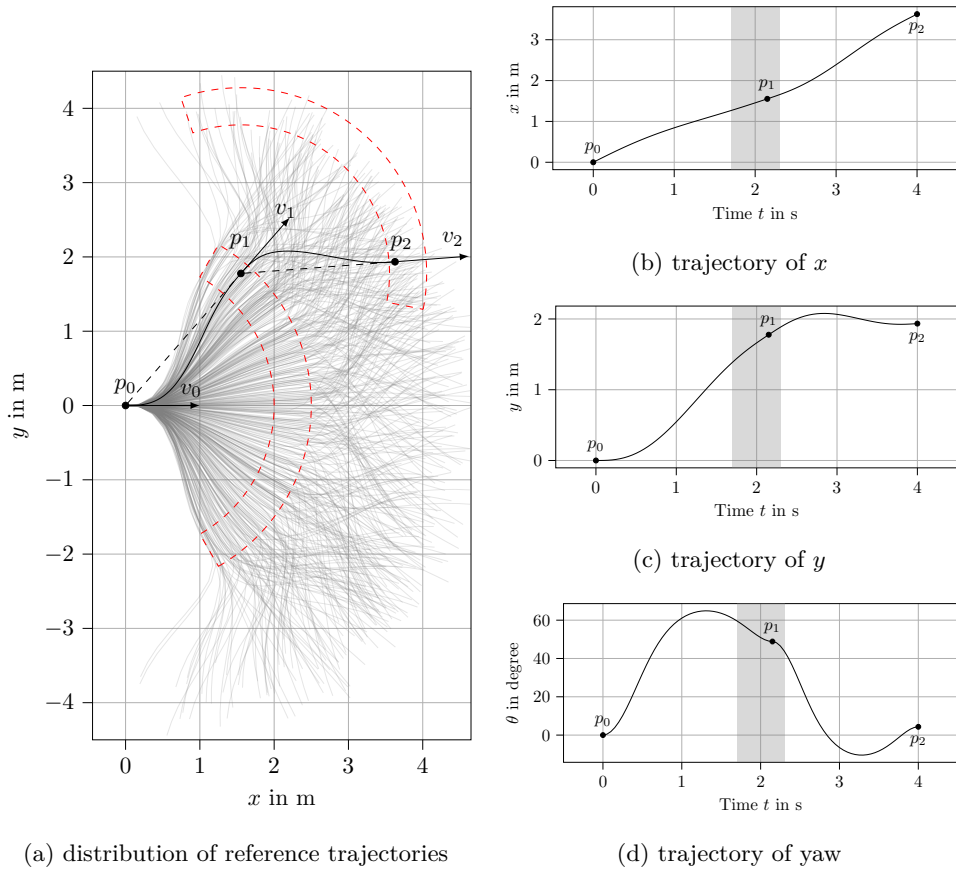


Fig. 11: The left subfigure shows the area generated by 500 randomly sampled reference trajectories used for tracking (depicted as grey lines), along with an example reference trajectory to illustrate the rules for generating trajectories (shown as a black line). The red dashed disks represent the distribution range for the position of the next point in the x - y plane, assuming the previous point is determined. The radial gap of the disk is 0.5 m, with an angular span $\pm 60^\circ$ centered around the tangent direction at the previous point. The right subfigure illustrates the temporal evolution of the example reference trajectory, showing its x , y , and yaw components. The time points for generating points p_0 and p_2 are fixed. The grey areas in the right subfigures represent the time range for point p_1 , which is centered around $t = 2$ s with a permissible deviation of ± 0.3 s.

5.2.2 Gradient Estimation

In the context of the ant model, which is a system characterized by contacts and non-smooth motion, employing system identification methods as described in Section 5.1 is not applicable. Fortunately, the powerful parallel simulation capability of the

Isaac Gym environment allows us to easily estimate the system gradient $\mathcal{G}(u_t)$ using a stochastic finite difference method. At each iteration, we run n_{env} (here $n_{\text{env}} = 2000$) identical environments in parallel in addition to the nominal environment. The nominal input u_t , $t = 1, \dots, T$, is fed into the nominal environment, yielding the corresponding nominal output y_t . For the remaining parallel environments, normally distributed noise n_d with a mean of zero and a variance of one is added to the nominal input u_t (see Figure 2a), denoted as $\tilde{u}_{t,i}$, $i = 1, \dots, n_{\text{env}}$, resulting in the respective outputs $\tilde{y}_{t,i}$. Finally, we estimate the system gradient $\mathcal{G}(u_t)$ using least squares⁴:

$$\mathcal{G}(u_t)^\top = \begin{bmatrix} (\tilde{u}_{t,1} - u_t)^\top \\ (\tilde{u}_{t,2} - u_t)^\top \\ \vdots \\ (\tilde{u}_{t,n_{\text{env}}} - u_t)^\top \end{bmatrix}^\dagger \begin{bmatrix} (\tilde{y}_{t,1} - y_t)^\top \\ (\tilde{y}_{t,2} - y_t)^\top \\ \vdots \\ (\tilde{y}_{t,n_{\text{env}}} - y_t)^\top \end{bmatrix},$$

where we stack all inputs and outputs by columns respectively.

5.2.3 Neural Network with Pre-Trained Motion Patterns

In order to enable online learning with the ant model, we parameterize our networks as follows:

$$\pi_{\text{ff}}(\omega_{\text{ff}}; \zeta) = U\phi(\omega_{\text{ff}}; V^\top \zeta), \quad \pi_{\text{fb}} = 0,$$

where the matrices $U \in \mathbb{R}^{mq \times n_\sigma}$ and $V \in \mathbb{R}^{nq \times n_\sigma}$ represent linear transformation to a lower dimensional latent space and $\phi: \mathbb{R}^{n\omega_{\text{ff}}} \times \mathbb{R}^{n_\sigma} \rightarrow \mathbb{R}^{mq}$ is a neural network comprising one hidden layer. The matrices U and V are obtained through a pretraining process based on 45 trajectories. Further details about the pretraining process and obtaining the matrices U and V are included in Appendix C.

5.2.4 Experiments

In this experiment, we use a fully connected network with only one hidden layer containing 20 neurons. The hidden layer employs the ReLU activation function, while the output layer does not have an activation function. We employ different methods to train the network, and the parameters are shown in Table 6. The two experiments

Table 6: Parameters for training the ant model.

No.	Model	n_σ	Hidden Neurons	ϵ	α	η
1	π_{ff}	90	45	$+\infty$	-	Diminishing
2	π_{ff}	45	20	0.1	0.5	0.1

were conducted with over 1500 and 3500 iterations, respectively, and their convergence results are shown in Figure 12. We note that the loss of both algorithms eventually

⁴In the experiment, only the ants that remain upright until the end are considered for estimating the gradient.

converges to the same level with the same rate. However, it is important to emphasize that to ensure the convergence of the gradient descent method, its step size η_t must be carefully designed. In contrast, the quasi-Newton method demonstrates much stronger robustness to the step size selection. Finally, through this experiment, we demonstrate that in such complex cyber-physical system, even with a poor gradient estimate, our algorithms still ensure convergence and exhibit high robustness to modeling errors. It is important to emphasize that, unlike RL, which optimizes a feedback policy to enable the ant to move forward as fast as possible, our algorithms learn a feedforward model π_{ff} that allows the ant to track any reference trajectories sampled from the distribution $p_{y_{\text{ref}}}$, thereby truly enabling it to learn the skill of walking. Additionally, our algorithms are capable of continuously improving the tracking performance of the feedforward network through online learning during deployment.

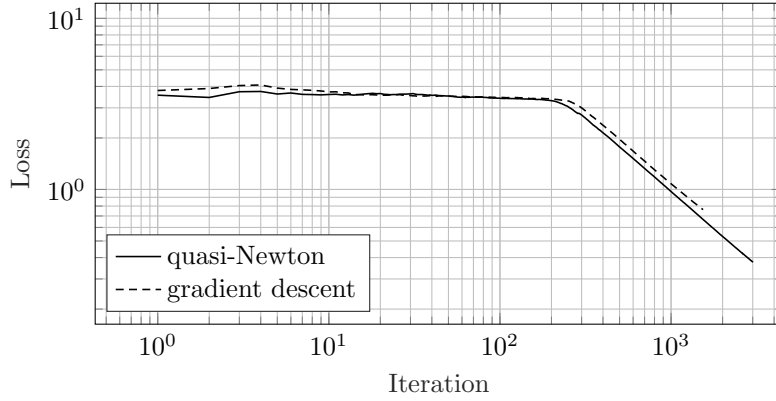


Fig. 12: The figure shows the convergence results of the gradient descent and quasi-Newton method. The gray line represents the average loss of the gradient descent method, and the black line indicates the average loss of the quasi-Newton method.

We select one of the trajectories in Figure 13 to demonstrate the tracking performance of the neural network trained by the quasi-Newton method. The left subfigure shows the tracking performance in the three-dimensional space, where the reference trajectory is set at a fixed height of 0.5 m. The right subfigures separately demonstrate the tracking performance of the model for the x , y , and yaw components of the trajectory.

5.3 Table Tennis Robot

In this experiment, we evaluate the effectiveness of our algorithms in a real-world cyber-physical system, which is a robotic arm actuated by pneumatic artificial muscles (PAMs) as shown in Figure 14. This robotic arm is designed for playing table tennis. The PAMs offer a high power-to-weight ratio enabling rapid movements, but also

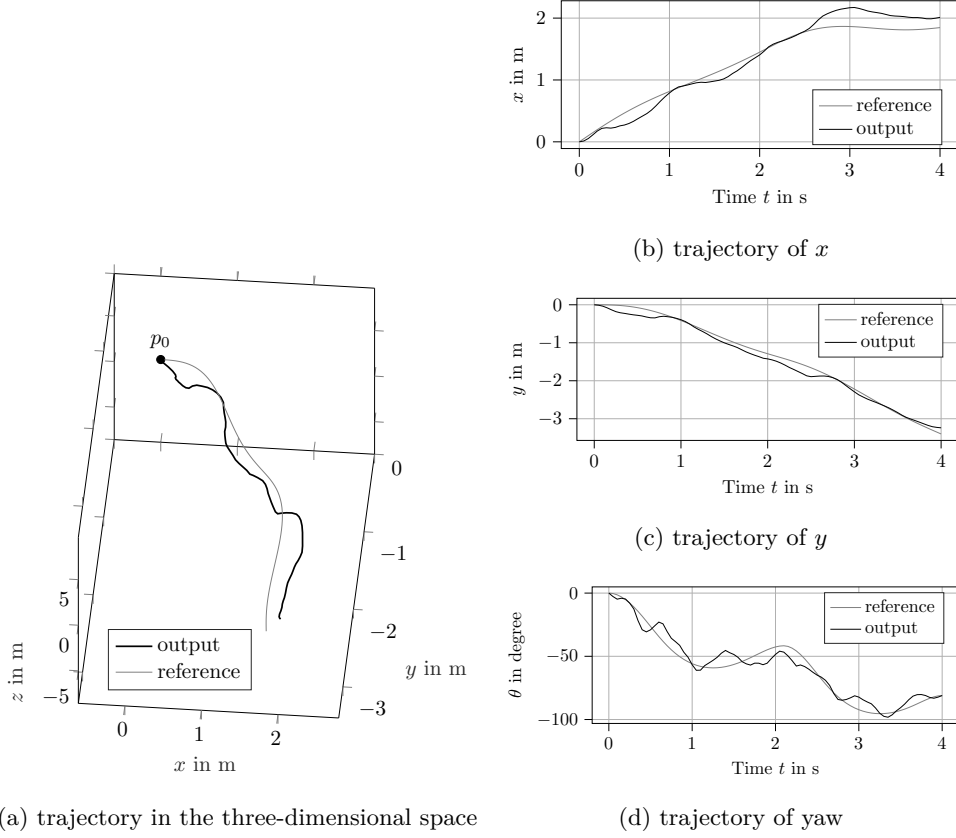


Fig. 13: The figure shows the tracking performance of the network trained by the quasi-Newton method on a single reference trajectory. The left subfigure illustrates the tracking effect of the network in the three-dimensional space, where the z -value of the reference trajectory is chosen to be 0.5 m. The right subfigures separately show the tracking performance of the network for the x , y , and yaw components.

introduce substantial nonlinearities to the system, making the precise control of this robotic arm particularly challenging.

The robot has four rotational degrees of freedom (DoF), each powered by a pair of PAMs. For more information about this robot, please refer to [Ma et al \(2022\)](#); [Büchler et al \(2022, 2016\)](#). In this experiment, we only consider learning the controller for the first three degrees of freedom, as the last degree of freedom can be accurately controlled with a PID controller.

5.3.1 Reference Trajectory Distribution

In this experiment, the distribution of the reference trajectories is tailored to the specific task of playing table tennis. First, we fix the initial posture p_{ini} of the robot,

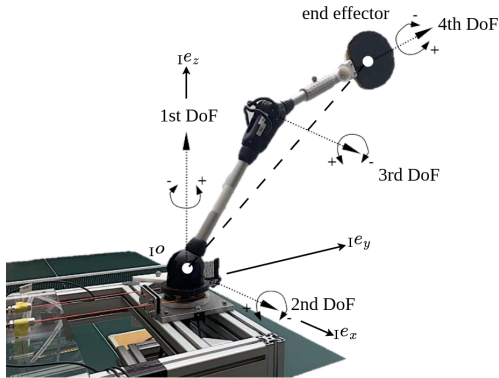


Fig. 14: The figure shows the structure of the robot arm. It has four rotational joints, and each joint is actuated by a pair of PAMs. The unit vectors $1e_x$, $1e_y$ and $1e_z$ together form the global coordinate system $\{I\}$ with $1O$ as the origin. For simplicity we consider only DoF 1-3, whereas DoF 4 is controlled with a PID controller.

and then determine the interception point p_{int} based on the incoming trajectory of the table tennis ball. The robot moves from the initial posture to the interception point and then returns to the initial posture. Each trajectory is planned within a polar coordinate system using a minimum jerk trajectory that connects p_{ini} and p_{int} . For more detailed information and the specific form of the trajectory, please refer to [Ma et al \(2022, 2023\)](#).

5.3.2 Gradient Estimation

Each degree of freedom is highly coupled with the others. However, for estimating the gradient, we disregard the coupling between each degree of freedom, thereby decomposing the system into three independent subsystems. This allows for the gradient estimation for each degree of freedom separately. The input for each degree of freedom consists of the pressure values from two artificial muscles, and the output is the angle of the degree of freedom. We further reduce the number of inputs by setting a baseline pressure and controlling the pressure difference between the two artificial muscles and the baseline. Subsequently, we use the method described in Section 5.1 to identify the transfer function for each simplified degree of freedom in the frequency domain and use this to estimate a static gradient \mathcal{G}^i , $i = 1, 2, 3$ for each degree of freedom. Please refer to [Ma et al \(2022\)](#) for details on the system identification and the construction of the approximate gradient.

5.3.3 Network and Input Structure

We construct three structurally identical linear network models, π_{ff}^i , $i = 1, 2, 3$ as in Section 5.1. Although the coupling between different degrees of freedom is ignored for the gradient estimation, the coupling is accounted for by the online learning. Therefore, we use the reference trajectories of all three degrees of freedom as inputs to each

linear model. The method for generating the inputs is also described in Section 5.1, where $h = 100$.

5.3.4 Experiments

The reference trajectories are derived from past interceptions of table tennis balls, and we use 30 reference trajectories for training. In our online learning approach, we randomly sample a reference trajectory without replacement. Once every reference trajectory has been executed we start a new epoch, where we again sample one trajectory at random without replacement.

The convergence of the online learning is shown in Figure 15, with each epoch distinguished by vertical dashed lines. It is observed that the average tracking errors of all three linear models converge with the same rate. This suggests that through the training, the linear models are capable of capturing the coupling effects between different degrees of freedom. It is important to emphasize that even with a rough estimate of the gradient, our algorithm achieves rapid convergence and maintains stability in a highly complex nonlinear system. This not only underlines the robustness of our algorithm against modeling errors but also provides empirical evidence of its performance on real-world systems.

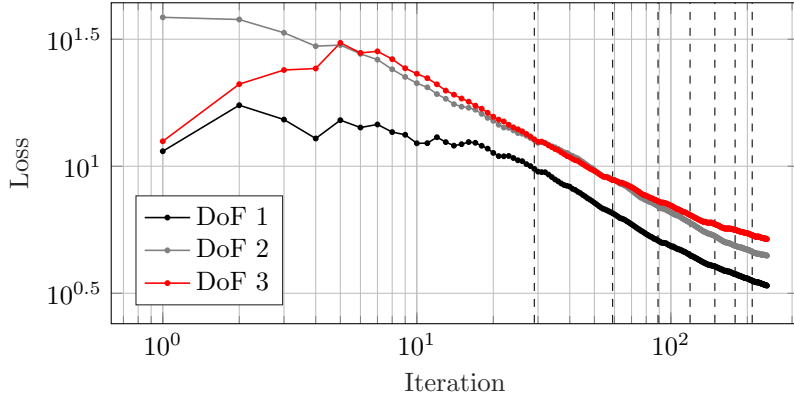


Fig. 15: This figure illustrates the average tracking error for each degree of freedom. Each independent linear model is trained by a pseudo-online learning approach, wherein each trajectory is randomly sampled without replacement in every epoch. A total of 30 reference trajectories are available for training in each epoch. Each epoch is distinguished in the figure by vertical dashed lines.

We select one trajectory from the last training epoch to demonstrate the tracking performance of the linear models. In Figure 16, the left subfigure shows the tracking performance of the tip of the robot in three-dimensional space. The right subfigures separately show the tracking performance for each degree of freedom.

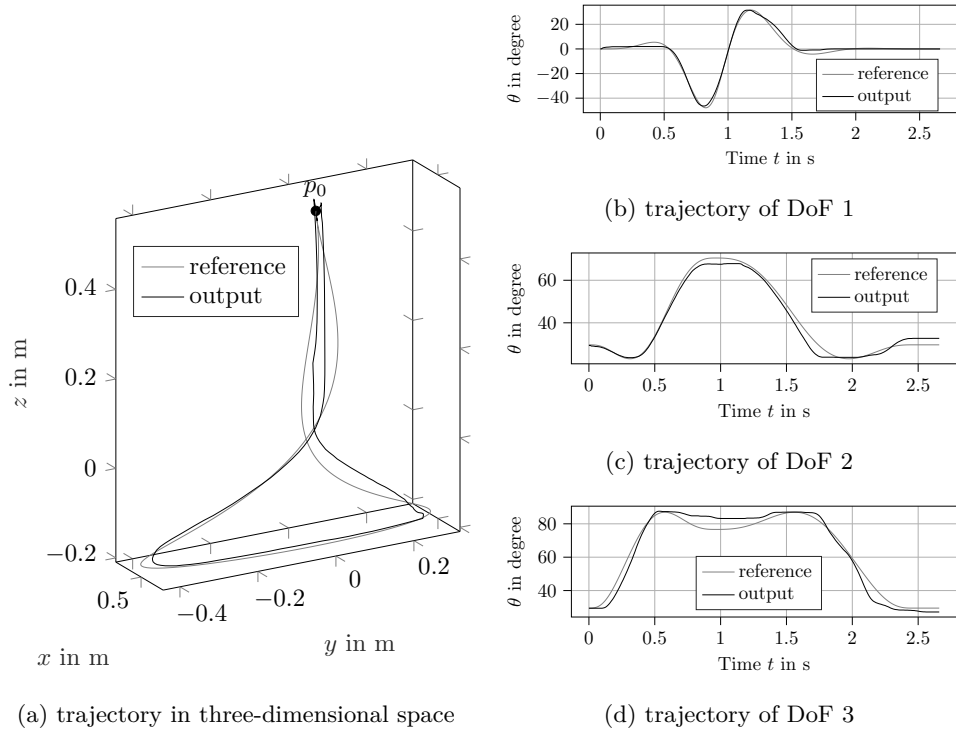


Fig. 16: The figure demonstrates the tracking performance of a reference trajectory from the last training epoch. The left subfigure shows the tracking performance of the tip of the robot in three-dimensional space. The right subfigures separately show the tracking performance for each degree of freedom.

6 Conclusions

In this article, we propose a novel gradient-based online learning framework derived from a trust-region approach, operating under the assumptions that the loss functions are smooth but not required to be convex. Thanks to gradient information that is incorporated within the algorithm, we obtain a sample efficient online learning approach that is applicable to cyber-physical and robotic systems. The framework presented in this article includes a stochastic optimization algorithm, various designs for neural networks and input structures for feedforward and feedback control scenarios. We have not only theoretically proven the convergence of the algorithm without relying on convexity, but also evaluated the effectiveness of our proposed framework through a wide range of examples, including numerical experiments, simulation experiments, and real-world implementations. These experiments highlight fast convergence of our algorithms and robustness against modeling errors. Furthermore, they provide empirical evidence that this algorithm can be deployed in real-world applications in the future.

Acknowledgements. Hao Ma and Michael Muehlebach thank the German Research Foundation, the Branco Weiss Fellowship, administered by ETH Zurich, and the Center for Learning Systems for the funding support.

Disclosures and Declarations

Funding. This work received funding from the German Research Foundation, the Branco Weiss Fellowship, administered by ETH Zurich, and the Center for Learning Systems.

Conflict of interest/Competing interests. The authors have no competing interests to declare that are relevant to the content of this article.

Ethics approval and consent to participate. Not applicable.

Consent for publication. Not applicable.

Data availability. Not applicable.

Code availability. Not applicable.

Author contribution. M. Michael and H. Ma conceived the original idea. The theoretical analysis presented in the paper was contributed to by M. Zeilinger, M. Michael and H. Ma. H. Ma performed all the coding and experiments. M. Zeilinger and M. Michael provided experimental concepts and guided the experiments based on the results. The initial draft of the manuscript was jointly prepared by M. Michael and H. Ma. The manuscript was revised based on valuable feedback from M. Zeilinger and was submitted with the joint agreement of M. Zeilinger and M. Michael.

Appendix A Proof of Theorem 2.1

In this appendix we will prove Theorem 2.1. First of all, we show that Assumption 2.4 implies the following inequality:

$$|\mathbb{E}_\zeta [\mathcal{F}(\omega_t; \zeta) | \omega_t] - \mathbb{E}_\zeta [\nabla f(\omega_t; \zeta) | \omega_t]|_{A_{t-1}^{-1}}^2 \leq \kappa^2 |\mathbb{E}_\zeta [\nabla f(\omega; \zeta) | \omega]|_{A_{t-1}^{-1}}^2.$$

Lemma A.1. *Let*

$$\lambda_{\max}(P) |y - x|^2 \leq \kappa^2 \lambda_{\min}(P) |x|^2 \tag{A1}$$

be satisfied for all $x, y \in \mathbb{R}^n$, $\kappa \in [0, 1)$, and for a positive definite matrix $P \in \mathbb{R}^{n \times n}$, then the following inequality holds

$$|y - x|_P^2 \leq \kappa^2 |x|_P^2.$$

Proof. We prove Lemma A.1 via a contradiction argument. We first assume that there exists $x, y \in \mathbb{R}^n$ such that (A1) is satisfied and the following inequality holds

$$|y - x|_P^2 > \kappa^2 |x|_P^2,$$

which implies that

$$\lambda_{\max}(P) |y - x|^2 \geq |y - x|_P^2 > \kappa^2 |x|_P^2 \geq \kappa^2 \lambda_{\min}(P) |x|^2.$$

Then we have

$$\lambda_{\max}(P) |y - x|^2 > \kappa^2 \lambda_{\min}(P) |x|^2,$$

which contradicts (A1). This concludes the proof of Lemma A.1. \square

We note that a key difficulty in the proof of Theorem 2.1 is that the stochastic gradients and the matrices A_t^{-1} are dependent random variables. We will therefore in a first step, represent the inverse of the matrix A_t using A_{t-1}^{-1} in order to decouple the dependency.

Proposition A.1. *Consider the sequence of pseudo-Hessian matrices A_t obtained according to Algorithm 2. Then, the following relationship between A_{t-1}^{-1} and A_t^{-1} holds for all $t \geq 2$,*

$$A_t^{-1} = \frac{t}{t-1} A_{t-1}^{-1} - \frac{t}{(t-1)^2} R_t \left(\mathbf{I} + \frac{1}{t-1} R_t \right)^{-1} A_{t-1}^{-1},$$

where

$$R_t := A_{t-1}^{-1} \left(\frac{\mathcal{L}_t^T \nabla_y^2 l(y_t; \zeta_t) \mathcal{L}_t}{\epsilon} + \frac{\alpha \nabla_{\omega} \pi(\omega_t, y_t; \zeta_t) \nabla_{\omega} \pi(\omega_t, y_t; \zeta_t)^T}{\epsilon} + \mathbf{I} \right), \quad \zeta_t \stackrel{\text{i.i.d.}}{\sim} p_{\zeta}.$$

Proof. We start with the definition of A_t ,

$$\begin{aligned} A_t &= \frac{t-1}{t} A_{t-1} + \frac{1}{t} \frac{\mathcal{L}_t^T \nabla_y^2 l(y_t; \zeta_t) \mathcal{L}_t + \alpha \nabla_{\omega} \pi(\omega_t, y_t; \zeta_t) \nabla_{\omega} \pi(\omega_t, y_t; \zeta_t)^T}{\epsilon} + \frac{1}{t} \mathbf{I} \\ &= \frac{t-1}{t} A_{t-1} \left(\mathbf{I} + \frac{1}{t-1} R_t \right), \quad \forall t \geq 2. \end{aligned}$$

In addition, we notice that the matrix A_t is always positive definite due to the addition of the identity matrix \mathbf{I} . Therefore, we can calculate the inverse of A_t as follows:

$$\begin{aligned} A_t^{-1} &= \frac{t}{t-1} \left(\mathbf{I} + \frac{1}{t-1} R_t \right)^{-1} A_{t-1}^{-1} \\ &= \frac{t}{t-1} \left[\mathbf{I} - \frac{1}{t-1} R_t \left(\mathbf{I} + \frac{1}{t-1} R_t \right)^{-1} \right] A_{t-1}^{-1} \\ &= \frac{t}{t-1} A_{t-1}^{-1} - \frac{t}{(t-1)^2} R_t \left(\mathbf{I} + \frac{1}{t-1} R_t \right)^{-1} A_{t-1}^{-1}, \quad \forall t \geq 2. \end{aligned}$$

\square

We now prove Theorem 2.1.

Proof. We start by analyzing the decrease of $F(\omega_{t+1})$ conditioned on $\omega_{1:t}$, where we substitute the iterative scheme in Algorithm 2. We obtain the following result:

$$\begin{aligned}
& \mathbb{E}_{\zeta_t} [F(\omega_{t+1}) - F(\omega_t) | \omega_{1:t}] = \mathbb{E}_{\zeta_t} [F(\omega_t - \eta_t A_t^{-1} \mathcal{F}(\omega_t; \zeta_t)) - F(\omega_t) | \omega_{1:t}] \\
& \leq \mathbb{E}_{\zeta_t} \left[-\eta_t \nabla F(\omega_t)^\top A_t^{-1} \mathcal{F}(\omega_t; \zeta_t) + \frac{L\eta_t^2}{2} |A_t^{-1} \mathcal{F}(\omega_t; \zeta_t)|^2 \middle| \omega_{1:t} \right] \\
& \leq -\mathbb{E}_{\zeta_t} [\eta_t \nabla F(\omega_t)^\top A_t^{-1} \mathcal{F}(\omega_t; \zeta_t) | \omega_{1:t}] + \frac{LH^2\eta_t^2}{2},
\end{aligned} \tag{A2}$$

where the first inequality arises from the L -smoothness of $F(\omega)$, while the second inequality stems from Assumption 2.2 the fact that $1/\lambda \leq \|A_t^{-1}\| \leq 1$:

$$\mathbb{E}_{\zeta_t} \left[|A_t^{-1} \mathcal{F}(\omega_t; \zeta_t)|^2 \middle| \omega_{1:t} \right] \leq \|A_t^{-1}\|^2 \mathbb{E}_{\zeta_t} \left[|\mathcal{F}(\omega_t; \zeta_t)|^2 \middle| \omega_{1:t} \right] \leq H^2,$$

where $\|\cdot\|$ denotes the spectral norm of a matrix.

Next we rearrange (A2) and get the following expression:

$$\mathbb{E}_{\zeta_t} [\eta_t \nabla F(\omega_t)^\top A_t^{-1} \mathcal{F}(\omega_t; \zeta_t) | \omega_{1:t}] \leq \mathbb{E}_{\zeta_t} [F(\omega_t) - F(\omega_{t+1}) | \omega_{1:t}] + \frac{LH^2\eta_t^2}{2}. \tag{A3}$$

By substituting the result of Proposition A.1 into the term on the left-hand side, we have the following result:

$$\begin{aligned}
& \eta_t \nabla F(\omega_t)^\top A_t^{-1} \mathcal{F}(\omega_t; \zeta_t) \\
& = \eta_t \nabla F(\omega_t)^\top \left(\frac{t}{t-1} A_{t-1}^{-1} - \frac{t}{(t-1)^2} R_t \left(\mathbf{I} + \frac{1}{t-1} R_t \right)^{-1} A_{t-1}^{-1} \right) \mathcal{F}(\omega_t; \zeta_t) \\
& = \frac{\eta_t t}{t-1} \nabla F(\omega_t)^\top A_{t-1}^{-1} (\nabla f(\omega_t; \zeta_t) - \nabla f(\omega_t; \zeta_t) + \mathcal{F}(\omega_t; \zeta_t)) \\
& \quad - \frac{\eta_t t}{(t-1)^2} \nabla F(\omega_t)^\top R_t \left(\mathbf{I} + \frac{1}{t-1} R_t \right)^{-1} A_{t-1}^{-1} \mathcal{F}(\omega_t; \zeta_t) \\
& \geq \frac{\eta_t t}{t-1} \nabla F(\omega_t)^\top A_{t-1}^{-1} (\nabla f(\omega_t; \zeta_t) - \nabla f(\omega_t; \zeta_t) + \mathcal{F}(\omega_t; \zeta_t)) \\
& \quad - \frac{\eta_t \lambda}{t-1} |\nabla F(\omega_t)| |\mathcal{F}(\omega_t; \zeta_t)|, \quad \forall t \geq 2.
\end{aligned} \tag{A4}$$

The last inequality is obtained due to the following facts:

$$\|R_t\| \leq \|A_{t-1}^{-1}\| \left\| \frac{\mathcal{L}_t^\top \nabla_y^2 l(y_t; \zeta_t) \mathcal{L}_t}{\epsilon} + \frac{\alpha \pi_\omega(\omega_t, y_t; \zeta_t) \pi_\omega(\omega_t, y_t; \zeta_t)^\top}{\epsilon} + \mathbf{I} \right\| \leq \lambda,$$

and

$$\begin{aligned} & \left\| \left(\mathbf{I} + \frac{1}{t-1} R_t \right)^{-1} A_{t-1}^{-1} \right\| \\ &= \left\| \left(A_{t-1} + \frac{1}{t-1} \left(\frac{\mathcal{L}_t^T \nabla_y^2 l(y_t; \zeta_t) \mathcal{L}_t}{\epsilon} + \frac{\alpha \pi_\omega(\omega_t, y_t; \zeta_t) \pi_\omega(\omega_t, y_t; \zeta_t)^T}{\epsilon} + \mathbf{I} \right) \right)^{-1} \right\| \\ & \leq \frac{t-1}{t}. \end{aligned}$$

For $t = 1$ we have

$$\begin{aligned} & \eta_1 \nabla F(\omega_1)^T \left(\frac{\mathcal{L}_1^T \nabla_y^2 l(y_1; \zeta_1) \mathcal{L}_1}{\epsilon} + \frac{\alpha \pi_\omega(\omega_1, y_1; \zeta_1) \pi_\omega(\omega_1, y_1; \zeta_1)^T}{\epsilon} + \mathbf{I} \right)^{-1} \mathcal{F}(\omega_1; \zeta_1) \\ &= \eta_1 \nabla F(\omega_1)^T \left(\mathbf{I} - R_1 (\mathbf{I} + R_1)^{-1} \right) \mathcal{F}(\omega_1; \zeta_1) \\ &\geq \eta_1 \nabla F(\omega_1)^T (\nabla f(\omega_1; \zeta_1) - \nabla f(\omega_1; \zeta_1) + \mathcal{F}(\omega_1; \zeta_1)) - \eta_1 \lambda |\nabla F(\omega_1)| |\mathcal{F}(\omega_1; \zeta_1)|, \end{aligned} \tag{A5}$$

where

$$R_1 := \frac{\mathcal{L}_1^T \nabla_y^2 l(y_1; \zeta_1) \mathcal{L}_1}{\epsilon} + \frac{\alpha \nabla_\omega \pi(\omega_1, y_1; \zeta_1) \nabla_\omega \pi(\omega_1, y_1; \zeta_1)^T}{\epsilon} + \mathbf{I}, \quad \zeta_1 \stackrel{\text{i.i.d.}}{\sim} p_\zeta.$$

We now substitute the result of (A4) into (A3) and rearrange the terms. We evaluate conditional expectations on both sides as follows:

$$\begin{aligned} & \frac{\eta_t t}{t-1} \mathbb{E}_{\zeta_t} [\nabla F(\omega_t)^T A_{t-1}^{-1} (\nabla f(\omega_t; \zeta_t) - \nabla f(\omega_t; \zeta_t) + \mathcal{F}(\omega_t; \zeta_t)) | \omega_{1:t}] \\ &= \frac{\eta_t t}{t-1} \nabla F(\omega_t)^T A_{t-1}^{-1} \nabla F(\omega_t) - \frac{\eta_t t}{t-1} \mathbb{E}_{\zeta_t} [\nabla F(\omega_t)^T A_{t-1}^{-1} (\nabla f(\omega_t; \zeta_t) - \mathcal{F}(\omega_t; \zeta_t)) | \omega_{1:t}]. \end{aligned}$$

Then, we apply the Peter-Paul inequality and Lemma A.1 to the second term, and get the following result:

$$\begin{aligned} & \mathbb{E}_{\zeta_t} [\nabla F(\omega_t)^T A_{t-1}^{-1} (\nabla f(\omega_t; \zeta_t) - \mathcal{F}(\omega_t; \zeta_t)) | \omega_{1:t}] \\ &= \nabla F(\omega_t)^T A_{t-1}^{-1} (\nabla F(\omega_t) - \mathbb{E}_{\zeta_t} [\mathcal{F}(\omega_t; \zeta_t) | \omega_{1:t}]) \\ &\leq \frac{\kappa}{2} \nabla F(\omega_t)^T A_{t-1}^{-1} \nabla F(\omega_t) + \frac{1}{2\kappa} |\nabla F(\omega_t) - \mathbb{E}_{\zeta_t} [\mathcal{F}(\omega_t; \zeta_t) | \omega_{1:t}]|_{A_{t-1}^{-1}}^2 \\ &\leq \frac{\kappa}{2} |\nabla F(\omega_t)|_{A_{t-1}^{-1}}^2 + \frac{\kappa}{2} |\nabla F(\omega_t)|_{A_{t-1}^{-1}}^2 \\ &= \kappa |\nabla F(\omega_t)|_{A_{t-1}^{-1}}^2. \end{aligned}$$

Meanwhile, we have

$$\mathbb{E}_{\zeta_t} [|\nabla F(\omega_t)| |\mathcal{F}(\omega_t; \zeta_t)| | \omega_{1:t}] \leq \mathbb{E}_{\zeta_t} [|\nabla F(\omega_t)| | \omega_{1:t}] \mathbb{E}_{\zeta_t} [|\mathcal{F}(\omega_t; \zeta_t)| | \omega_{1:t}] \leq H^2,$$

as a result of Jensen's inequality. At last, we have

$$\frac{\eta_t t}{t-1} \mathbb{E}_{\zeta_t} [\nabla F(\omega_t)^\top A_{t-1}^{-1} \mathcal{F}(\omega_t; \zeta_t) | \omega_{1:t}] \geq \frac{\eta_t t (1-\kappa)}{t-1} |\nabla F(\omega_t)|_{A_{t-1}^{-1}}^2 - \frac{\eta_t H^2 \lambda}{t-1}.$$

For $t = 1$ we have

$$\eta_1 \mathbb{E}_{\zeta_1} [\nabla F(\omega_1)^\top \mathcal{F}(\omega_1; \zeta_1) | \omega_1] \geq \eta_1 (1-\kappa) |\nabla F(\omega_1)|^2 - \eta_1 H^2 \lambda.$$

Further, we get the following result by considering the expectation over all random variables on both sides in (A3):

$$\begin{aligned} (1-\kappa) \frac{\eta_t t}{t-1} \mathbb{E}_{\zeta_{1:T}} [|\nabla F(\omega_t)|_{A_{t-1}^{-1}}^2] \\ \leq \mathbb{E}_{\zeta_{1:T}} [F(\omega_t)] - \mathbb{E}_{\zeta_{1:T}} [F(\omega_{t+1})] + \frac{LH^2 \eta_t^2}{2} + \frac{\eta_t H^2 \lambda}{t-1}, \quad \forall t \geq 2. \quad (\text{A6}) \end{aligned}$$

We note that

$$\mathbb{E}_{\zeta_{1:T}} [|\nabla F(\omega_t)|_{A_t^{-1}}^2] \leq \frac{t}{t-1} \mathbb{E}_{\zeta_{1:T}} [|\nabla F(\omega_t)|_{A_{t-1}^{-1}}^2], \quad \forall t \geq 2,$$

and

$$\mathbb{E}_{\zeta_{1:T}} [|\nabla F(\omega_1)|_{A_1^{-1}}^2] \leq \mathbb{E}_{\zeta_{1:T}} [|\nabla F(\omega_1)|^2].$$

In the following, we exploit the fact that the step size is constant, that is, $\eta_t = \eta$ for all $t \geq 1$. As a consequence, (A6) can be rewritten as follows:

$$\begin{aligned} (1-\kappa) \mathbb{E}_{\zeta_{1:T}} [|\nabla F(\omega_t)|_{A_t^{-1}}^2] \\ \leq \frac{\mathbb{E}_{\zeta_{1:T}} [F(\omega_t)] - \mathbb{E}_{\zeta_{1:T}} [F(\omega_{t+1})]}{\eta} + \frac{LH^2 \eta}{2} + \frac{H^2 \lambda}{t-1}, \quad \forall t \geq 2. \end{aligned}$$

By summing up the above equation and including the case $t = 1$ we get the following result:

$$\begin{aligned} (1-\kappa) \sum_{t=1}^T \mathbb{E}_{\zeta_{1:T}} [|\nabla F(\omega_t)|_{A_t^{-1}}^2] \\ \leq \frac{F(\omega_1) - F(\omega^*)}{\eta} + \frac{TLH^2 \eta}{2} + H^2 \lambda \sum_{t=1}^T a_t, \quad \forall t \geq 1, \end{aligned}$$

where we notice that $F(\omega^*) \leq \mathbb{E}_{\zeta_{1:T}} [F(\omega_{T+1})]$ always holds since ω^* denotes the global minimum, and a_t is defined as $a_1 = 1$, $a_t = 1/t-1$ for $t \geq 2$. The above equation can be further simplified due to the fact that $F(\omega^*) \geq 0$:

$$(1 - \kappa) \sum_{t=1}^T \mathbb{E}_{\zeta_{1:T}} \left[|\nabla F(\omega_t)|_{A_t^{-1}}^2 \right] \leq \frac{F(\omega_1)}{\eta} + \frac{TLH^2\eta}{2} + H^2\lambda \sum_{t=1}^T a_t, \quad \forall t \geq 1. \quad (\text{A7})$$

The sum over a_t is bounded as follows:

$$\begin{aligned} \sum_{t=1}^T a_t &\leq \int_2^T \frac{1}{t-1} dt + 2 \\ &= \ln(T-1) + 2 \\ &\leq \ln T + 2, \quad \forall T \geq 1. \end{aligned} \quad (\text{A8})$$

We substitute (A8) into (A7) and calculate its average value as follows:

$$(1 - \kappa) \frac{1}{T} \sum_{t=1}^T \mathbb{E}_{\zeta_{1:T}} \left[|\nabla F(\omega_t)|_{A_t^{-1}}^2 \right] \leq \frac{F(\omega_1)}{\eta T} + \frac{LH^2\eta}{2} + \frac{\lambda H^2 (\ln T + 2)}{T}. \quad (\text{A9})$$

We set the first two terms on the right-hand side to be equal by choosing the step size appropriately,

$$\frac{F(\omega_1)}{\eta T} = \frac{LH^2\eta}{2} \Leftrightarrow \eta = \sqrt{\frac{2F(\omega_1)}{LH^2T}}.$$

This yields the following result:

$$\frac{1 - \kappa}{T} \sum_{t=1}^T \mathbb{E}_{\zeta_{1:T}} \left[|\nabla F(\omega_t)|_{A_t^{-1}}^2 \right] \leq \sqrt{\frac{2LH^2F(\omega_1)}{T}} + \frac{\lambda H^2 (\ln T + 2)}{T},$$

which is dominated by the first term on the right-hand side of the inequality for large T . It also implies that the average expected gradient will converge to zero at a rate of $\mathcal{O}(1/\sqrt{T})$. \square

Appendix B Derivation of Trust-Region Approach

In this appendix, we will present in detail the necessary intermediate steps used to derive the results in Section 3. We start from the local approximation of the function

$M(v, \omega)$

$$\begin{aligned}
M(v, \omega) = & \underbrace{f(\omega) + \nabla f(\omega)^\top (v - \omega) + \frac{1}{2} (v - \omega)^\top \nabla^2 f(\omega) (v - \omega)}_{\text{second order Taylor expansion}} \\
& + \underbrace{\frac{\alpha}{2} |\pi(v) - \pi(\omega)|^2}_{\text{Term 1}} + \underbrace{\frac{\epsilon}{2} |v - \omega|^2}_{\text{Term 2}}. \quad (\text{B10})
\end{aligned}$$

To obtain (13), it is important to note that, as specified in (B10), calculating the gradient and Hessian matrix of the loss function f is essential, which can be expressed as follows:

$$\begin{aligned}
\nabla f(\omega) &= \frac{\partial y^\top}{\partial \omega} \nabla_y l(y; \zeta), \\
\nabla^2 f(\omega) &= \frac{\partial^2 y^\top}{\partial \omega^2} \nabla_y l(y; \zeta) + \frac{\partial y^\top}{\partial \omega} \nabla_y^2 l(y; \zeta) \frac{\partial y}{\partial \omega},
\end{aligned} \quad (\text{B11})$$

where we introduce

$$\frac{\partial y}{\partial \omega} \approx \mathcal{L} = \left(\mathbf{I} - \mathcal{G}(u) \frac{\partial \pi(\omega, y; \zeta)}{\partial y} \right)^\dagger \mathcal{G}(u) \frac{\partial \pi(\omega, y; \zeta)}{\partial \omega},$$

and assume

$$\frac{\partial^2 y}{\partial \omega^2} \approx 0.$$

Then, (B10) can be formulated as follows:

$$\begin{aligned}
M(v, \omega) = & f(\omega) + (v - \omega)^\top \mathcal{L}^\top \nabla_y l(y; \zeta) + \frac{1}{2} (v - \omega)^\top \mathcal{L}^\top \nabla_y^2 l(y; \zeta) \mathcal{L} (v - \omega) \\
& + \frac{\alpha}{2} |\pi(v) - \pi(\omega)|^2 + \frac{\epsilon}{2} |v - \omega|^2.
\end{aligned}$$

We further perform a Taylor expansion of $\pi(v)$ around $\pi(\omega)$, that is,

$$\pi(v) = \pi(\omega) + \left. \frac{\partial \pi(\omega)}{\partial \omega} \right|_{\omega} (v - \omega) + \text{HOT},$$

where HOT denotes the remaining higher order term. This yields (13).

To obtain (14), we calculate the expectation of $M(v, \omega)$ as follows:

$$\begin{aligned}
\mathbb{E}_\zeta [M(v, \omega)|\omega] &= \underbrace{\int f(\omega; \xi) p_\zeta(\xi) d\xi}_{F(\omega)} + (v - \omega)^\top \int \mathcal{L}(\xi)^\top \nabla_y l(y; \xi) p_\zeta(\xi) d\xi \\
&+ \frac{1}{2} (v - \omega)^\top \underbrace{\int \mathcal{L}(\xi)^\top \nabla_y^2 l(y; \xi) \mathcal{L}(\xi) p_\zeta(\xi) d\xi}_{\epsilon \Sigma_1} (v - \omega) \\
&+ \frac{\alpha}{2} (v - \omega)^\top \underbrace{\int \nabla_\omega \pi(\omega; \xi) \nabla_\omega \pi(\omega; \xi)^\top p_\zeta(\xi) d\xi}_{\epsilon \Sigma_2} (v - \omega) \\
&+ \frac{\epsilon}{2} (v - \omega)^\top (v - \omega). \quad (\text{B12})
\end{aligned}$$

Appendix C Pretraining Process

In this appendix, we will briefly explain the pretraining process that is used in Section 5.2. The matrices U and V are obtained through the singular value decomposition of the matrix R :

$$R = U \text{diag}(\sigma) V^\top,$$

where the matrix R is derived by solving the following ridge regression:

$$\min_{R \in \mathbb{R}^{m_q \times n_q}} \frac{1}{2} \sum_{i=1}^{n_{\text{ILC}}} |u_{\text{ref}, i} - R y_{\text{ref}, i}|^2 + \frac{\rho}{2} \|R\|_F^2,$$

where ρ is a positive constant, and $\|\cdot\|_F$ denotes the Frobenius norm. The ideal input u_{ref} represents the input required for accurately tracking a given reference trajectory y_{ref} . The ideal input is unknown, and we therefore employ iterative learning control (ILC) to approximate it (Ma et al, 2022; Hofer et al, 2019; Zughaihi et al, 2021; Mueller et al, 2012; Schoellig et al, 2012; Zughaihi et al, 2024). The variable n_{ILC} denotes the number of pre-trained trajectories using ILC. In this experiment, we sample 50 reference trajectories and get their corresponding ideal inputs using ILC, and each reference trajectory takes 200 to 300 iterations to obtain the ideal inputs. We then use 45 trajectories (90%) along with their ideal inputs to perform ridge regression. Figure C1 displays the distribution composed of all 50 reference trajectories used for pre-training in the left subfigure, whereas the right subfigure showcases the final training result of ILC for one reference trajectory as an example. The right subfigures illustrate the tracking performance of the corresponding x , y , and yaw components of this trajectory. We note that the tracking of the x and y components by the ILC is very effective; however, due to the presence of collisions, the tracking of the yaw component is slightly less accurate. Nevertheless, we consider this as a sufficiently

good ideal input for tracking the given reference trajectory, which is able to capture the motion patterns.

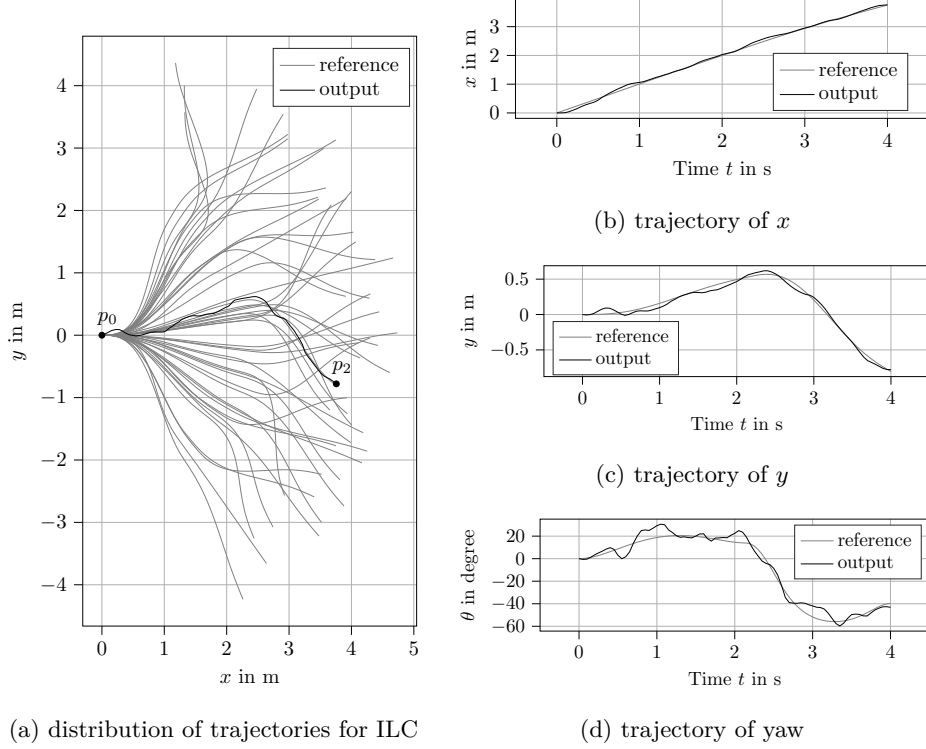


Fig. C1: The left subfigure shows the distribution of 50 randomly sampled reference trajectories used for pre-training (represented by gray lines), and illustrates the tracking performance of ILC with one of these trajectories (depicted as a black line). The right subfigures demonstrate the tracking performance of the ILC for the particular trajectory in the x , y , and yaw components.

References

- Abbasi-Yadkori Y, Szepesvári C, et al (2011) Regret Bounds for the Adaptive Control of Linear Quadratic Systems. In: Proceedings of Conference on Learning Theory, pp 1–26
- Abbasi-Yadkori Y, Bartlett P, Kanade V (2014) Tracking Adversarial Targets. In: Proceedings of International Conference on Machine Learning, pp 369–377
- Abbasi-Yadkori Y, Lazic N, Szepesvari C (2018) Model-Free Linear Quadratic Control via Reduction to Expert Prediction. arxiv 1804.06021:1–21

- Abernethy J, Hazan E, Rakhlin A (2009) Competing in the Dark: An Efficient Algorithm for Bandit Linear Optimization. In: Proceedings of Annual Conference on Learning Theory, pp 1–11
- Agarwal N, Bullins B, Hazan E (2017) Second-Order Stochastic Optimization for Machine Learning in Linear Time. *Journal of Machine Learning Research* 18(1):4148–4187
- Agarwal N, Bullins B, Hazan E, et al (2019) Online Control with Adversarial Disturbances. arXiv 1902.08721:1–15
- Amirouche F (2007) *Fundamentals of Multibody Dynamics: Theory and Applications*. Springer Science & Business Media, New York
- Anderson BDO (2005) Failures of Adaptive Control Theory and Their Resolution. *Communications in Information & Systems* 5(1):1–20
- Auer P, Cesa-Bianchi N, Fischer P (2002) Finite-Time Analysis of the Multiarmed Bandit Problem. *Machine Learning* 47(2-3):235–256
- Bellicoso CD, Jenelten F, Gehring C, et al (2018) Dynamic Locomotion Through Online Nonlinear Motion Optimization for Quadrupedal Robots. *Robotics and Automation Letters* 3(3):2261–2268
- Bottou L (2010) Large-Scale Machine Learning with Stochastic Gradient Descent. In: Proceedings of International Conference on Computational Statistics, pp 177–186
- Bottou L, Curtis FE, Nocedal J (2018) Optimization Methods for Large-Scale Machine Learning. *SIAM Review* 60(2):223–311
- Boyd SP, Vandenberghe L (2004) *Convex Optimization*. Cambridge University Press, Cambridge
- Bubeck S (2011) Introduction to Online Optimization. *Lecture Notes* 2(1):1–86
- Bubeck S (2012) Regret Analysis of Stochastic and Nonstochastic Multi-armed Bandit Problems. *Foundations and Trends in Machine Learning* 5(1):1–122
- Büchler D, Ott H, Peters J (2016) A Lightweight Robotic Arm with Pneumatic Muscles for Robot Learning. In: Proceedings of IEEE International Conference on Robotics and Automation, pp 4086–4092
- Büchler D, Guist S, Calandra R, et al (2022) Learning to Play Table Tennis From Scratch Using Muscular Robots. *IEEE Transactions on Robotics* 38(6):3850–3860
- Campi MC, Weyer E (2002) Finite Sample Properties of System Identification Methods. *IEEE Transactions on Automatic Control* 47(8):1329–1334

- Carè A, Csáji BC, Campi MC, et al (2018) Finite-Sample System Identification: An Overview and a New Correlation Method. *IEEE Control Systems Letters* 2(1):61–66
- Cesa-Bianchi N, Lugosi G (2006) *Prediction, Learning, and Games*. Cambridge University Press, Cambridge
- Cesa-Bianchi N, Conconi A, Gentile C (2005) A Second-Order Perceptron Algorithm. *SIAM Journal on Computing* 34(3):640–668
- Chan W, He Z, Moffat K, et al (2025) Robust Feedback Optimization with Model Uncertainty: A Regularization Approach. *arXiv 2503.24151:1–8*
- Chignoli M, Kim S (2021) Online Trajectory Optimization for Dynamic Aerial Motions of a Quadruped Robot. *arXiv 2110.06330:1–7*
- Cohen A, Hassidim A, Koren T, et al (2018) Online Linear Quadratic Control. *arXiv 1806.07104:1–22*
- Cohen A, Koren T, Mansour Y (2019) Learning Linear-Quadratic Regulators Efficiently with only \sqrt{T} Regret. *arXiv 1902.06223:1–30*
- Crammer K, Dekel O, Keshet J, et al (2006) Online Passive-Aggressive Algorithms. *Journal of Machine Learning Research* 7(19):551–585
- Crammer K, Kulesza A, Dredze M (2013) Adaptive Regularization of Weight Vectors. *Machine learning* 91(1):155–187
- Dean S, Mania H, Matni N, et al (2018) Regret Bounds for Robust Adaptive Control of the Linear Quadratic Regulator. *arXiv 1805.09388:1–47*
- Dekel O, Gilad-Bachrach R, Shamir O, et al (2012) Optimal Distributed Online Prediction Using Mini-Batches. *Journal of Machine Learning Research* 13(1):165–202
- Dosovitskiy A, Ros G, Codevilla F, et al (2017) CARLA: An Open Urban Driving Simulator. *arXiv 1711.03938:1–16*
- Dredze M, Crammer K, Pereira F (2008) Confidence-Weighted Linear Classification. In: *Proceedings of International Conference on Machine Learning*, pp 264–271
- Freund Y, Schapire RE (1997) A Decision-Theoretic Generalization of On-line Learning and an Application to Boosting. *Journal of Computer and System Sciences* 55(1):119–139
- Furrer F, Burri M, Achtelik M, et al (2016) RotorS—A Modular Gazebo MAV Simulator Framework. In: *Proceedings of Robot Operating System: The Complete Reference*, pp 595–625
- Geering HP (2007) *Optimal Control with Engineering Applications*. Springer, London

- Gentile C (2000) A New Approximate Maximal Margin Classification Algorithm. *Journal of Machine Learning Research* 2(1):213–242
- Gradu P, Hazan E, Minasyan E (2022) Adaptive Regret for Control of Time-Varying Dynamics. *arXiv* 2007.04393:1–43
- Hall EC, Willett RM (2015) Online Convex Optimization in Dynamic Environments. *IEEE Journal of Selected Topics in Signal Processing* 9(4):647–662
- Hazan E (2022) Introduction to Online Convex Optimization. MIT Press, Cambridge, MA
- Hazan E, Singh K (2025) Introduction to Online Control. *arXiv* 2211.09619:1–192
- Hazan E, Agarwal A, Kale S (2007a) Logarithmic regret algorithms for online convex optimization. *Machine Learning* 69(2):169–192
- Hazan E, Rakhlin A, Bartlett P (2007b) Adaptive Online Gradient Descent. In: *Proceedings of Advances in Neural Information Processing Systems*, pp 1–8
- Hazan E, Kakade SM, Singh K (2020) The Nonstochastic Control Problem. *arXiv* 1911.12178:1–12
- He Z, Bolognani S, Muehlebach M, et al (2024) Gray-Box Nonlinear Feedback Optimization. *arXiv* 2404.04355:1–16
- Heess N, TB D, Sriram S, et al (2017) Emergence of Locomotion Behaviours in Rich Environments. *arXiv* 1707.02286:1–14
- Ho D, Le HM, Doyle JC, et al (2021) Online Robust Control of Nonlinear Systems with Large Uncertainty. *arXiv* 2103.11055:1–58
- Hofer M, Spannagl L, D’Andrea R (2019) Iterative Learning Control for Fast and Accurate Position Tracking with an Articulated Soft Robotic Arm. In: *Proceedings of International Conference on Intelligent Robots and Systems*, pp 6602–6607
- Kalashnikov D, Irpan A, Pastor P, et al (2018) QT-Opt: Scalable Deep Reinforcement Learning for Vision-Based Robotic Manipulation. *arXiv* 1806.10293:1–23
- Kolev P, Martius G, Muehlebach M (2023) Online Learning under Adversarial Nonlinear Constraints. In: *Proceedings of Advances in Neural Information Processing Systems*, pp 53227–53238
- Laskin M, Lee K, Stooke A, et al (2020) Reinforcement Learning with Augmented Data. In: *Proceedings of Advances in Neural Information Processing Systems*, pp 19884–19895

- LeCun Y, Bottou L, Orr GB, et al (1998) Efficient BackProp. *Neural Networks: Tricks of the Trade* pp 9–50
- Li Y (2018) Deep Reinforcement Learning: An Overview. arXiv 1701.07274:1–85
- Li Y, Long P (1999) The Relaxed Online Maximum Margin Algorithm. *Machine Learning* 46(1):361–387
- Lin Y, Preiss JA, Xie F, et al (2024) Online Policy Optimization in Unknown Nonlinear Systems. arXiv 2404.13009:1–48
- Littlestone N, Warmuth MK (1994) The Weighted Majority Algorithm. *Information and Computation* 108(2):212–261
- Ljung L (2010) Perspectives on System Identification. *Annual Reviews in Control* 34(1):1–12
- Ma H, Büchler D, Schölkopf B, et al (2022) A Learning-based Iterative Control Framework for Controlling a Robot Arm with Pneumatic Artificial Muscles. In: *Proceedings of Robotics: Science and Systems*, pp 1–10
- Ma H, Büchler D, Schölkopf B, et al (2023) Reinforcement learning with model-based feedforward inputs for robotic table tennis. *Autonomous Robots* 47(8):1387–1403
- Makoviychuk V, Wawrzyniak L, Guo Y, et al (2021) Isaac Gym: High Performance GPU-Based Physics Simulation For Robot Learning. arXiv 2108.10470:1–32
- Mania H, Tu S, Recht B (2019) Certainty Equivalence is Efficient for Linear Quadratic Control. arXiv 1902.07826:1–28
- Martens J, Grosse R (2015) Optimizing Neural Networks with Kronecker-Factored Approximate Curvature. In: *Proceedings of International Conference on Machine Learning*, pp 2408–2417
- Martínez JM (1994) Local Minimizers of Quadratic Functions on Euclidean Balls and Spheres. *SIAM Journal on Optimization* 4(1):159–176
- McCord C, Queralta JP, Gia TN, et al (2019) Distributed Progressive Formation Control for Multi-Agent Systems: 2D and 3D deployment of UAVs in ROS/Gazebo with RotorS. In: *Proceedings of European Conference on Mobile Robots*, pp 1–6
- Muehlebach M (2023) Adaptive Decision-Making with Constraints and Dependent Losses: Performance Guarantees and Applications to Online and Nonlinear Identification. In: *Proceedings of IFAC World Congress*, pp 5107–5114
- Mueller FL, Schoellig AP, D’Andrea R (2012) Iterative Learning of Feed-Forward Corrections for High-Performance Tracking. In: *Proceedings of International Conference on Intelligent Robots and Systems*, pp 3276–3281

- Nesterov Y, Spokoiny V (2017) Random Gradient-Free Minimization of Convex Functions. *Foundations of Computational Mathematics* 17(2):527–566
- Neu G (2015) Explore no more: Improved high-probability regret bounds for non-stochastic bandits. In: *Proceedings of Advances in Neural Information Processing Systems*, pp 1–9
- Nocedal J, Wright SJ (2006) *Numerical Optimization*. Springer, New York
- Novikoff AB (1962) On Convergence Proofs on Perceptrons. In: *Proceedings of the Symposium on the Mathematical Theory of Automata*, pp 615–622
- Piazzzi A, Visioli A (1997) An Interval Algorithm for Minimum-Jerk Trajectory Planning of Robot Manipulators. In: *Proceedings of IEEE Conference on Decision and Control*, pp 1924–1927
- Pintelon R, Schoukens J (2012) *System Identification: A Frequency Domain Approach*. John Wiley & Sons, Hoboken NJ
- Reddi SJ, Kale S, Kumar S (2019) On the Convergence of Adam and Beyond. arXiv 1904.09237:1–23
- Ruder S (2017) An Overview of Gradient Descent Optimization Algorithms. arXiv 1609.04747:1–14
- Schoellig AP, Mueller FL, D’Andrea R (2012) Optimization-Based Iterative Learning for Precise Quadcopter Trajectory Tracking. *Autonomous Robots* 33(1):103–127
- Schulman J, Moritz P, Levine S, et al (2018) High-Dimensional Continuous Control Using Generalized Advantage Estimation. arXiv 1506.02438:1–14
- Shabana AA (1997) Flexible Multibody Dynamics: Review of Past and Recent Developments. *Multibody System Dynamics* 1(2):189–222
- Shah S, Dey D, Lovett C, et al (2017) AirSim: High-Fidelity Visual and Physical Simulation for Autonomous Vehicles. arXiv 1705.05065:1–14
- Shalev-Shwartz S (2012) Online Learning and Online Convex Optimization. *Foundations and Trends in Machine Learning* 4(2):107–194
- Shalev-Shwartz S, Singer Y (2007) A Primal-Dual Perspective of Online Learning Algorithms. *Machine Learning* 69(2):115–142
- Sorensen DC (1982) Newton’s Method with a Model Trust Region Modification. *SIAM Journal on Numerical Analysis* 19(2):409–426
- Sutton RS, Barto AG (2018) *Reinforcement Learning: An Introduction*. MIT Press, Cambridge MA

- Tobuschat P, Ma H, Büchler D, et al (2023) Data-Efficient Online Learning of Ball Placement in Robot Table Tennis. In: Proceeding of IEEE/RSJ International Conference on Intelligent Robots and Systems, pp 567–573
- Tsiamis A, Pappas GJ (2019) Finite Sample Analysis of Stochastic System Identification. In: Proceedings of IEEE Conference on Decision and Control, pp 3648–3654
- Wang K, Fei H, Kormushev P (2022) Fast Online Optimization for Terrain-Blind Bipedal Robot Walking With a Decoupled Actuated SLIP Model. *Frontiers in Robotics and AI* 9(1):1–11
- Yan YH, Zhao P, Zhou ZH (2023) Online Non-stochastic Control with Partial Feedback. *Journal of Machine Learning Research* 24(273):1–50
- Yuan Yx (2015) Recent Advances in Trust Region Algorithms. *Mathematical Programming* 151(1):249–281
- Zinkevich M (2003) Online Convex Programming and Generalized Infinitesimal Gradient Ascent. In: Proceedings of International Conference on Machine Learning, pp 928–936
- Zughaibi J, Hofer M, D’Andrea R (2021) A Fast and Reliable Pick-and-Place Application with a Spherical Soft Robotic Arm. In: Proceedings of International Conference on Soft Robotics, pp 599–606
- Zughaibi J, Nelson BJ, Muehlebach M (2024) Balancing a 3D Inverted Pendulum Using Remote Magnetic Manipulation. arXiv 2402.06012:1–8